The Astrophysical Journal, 591:461–485, 2003 July 1

MODELING SHOCK-ACCELERATED SOLAR ENERGETIC PARTICLES COUPLED TO INTERPLANETARY ALFVÉN WAVES

C. K. Ng[1] and D. V. Reames
NASA Goddard Space Flight Center, Greenbelt, MD 20771;
cheeng@milkyway.gsfc.nasa.gov, reames@milkyway.gsfc.nasa.gov

and

A. J. Tylka
E. O. Hulburt Center for Space Research, Code 7652, US Naval Research Laboratory, Washington, DC 20375;
allan.tylka@nrl.navy.mil
Received 2002 December 19; accepted 2003 March 12

ABSTRACT

We present an idealized model simulating the coupled evolution of the distributions of multispecies shock-accelerated energetic ions and interplanetary Alfvén waves in gradual solar energetic particle (SEP) events. Particle pitch-angle diffusion coefficients are expressed in terms of wave intensities, and wave growth rates in terms of momentum gradients of SEP distributions, by the same quasilinear theory augmented with resonance broadening. The model takes into consideration various physical processes: for SEPs, particle motion, magnetic focusing, scattering by Alfvén waves, solar wind convection, and adiabatic deceleration; for the waves, WKB transport and amplification by streaming SEPs. Shock acceleration is heuristically represented by continuous injection of prescribed spectra of SEPs at a moving shock front. We show the model predictions for two contrasting sets of SEP source spectra, fast weakening and softening in one case and long lasting and hard in the other. The results presented include concurrent time histories of multispecies SEP intensities and elemental abundance ratios, as well as sequential snapshots of the following: SEP intensity energy spectra, Alfvén wave spectra, particle mean free paths as functions of rigidity, and spatial profiles of SEP intensities and mean free paths. Wave growth plays a key role in both cases, although the magnitude of the wave growth differs greatly, and quite different SEP abundance variations are obtained. In these simulations, the maximum wave growth rate is large, but small relative to the wave frequency, and everywhere the total wave magnetic energy density remains small relative to that of the background magnetic field. The simulations show that, as the energetic protons stream outward, they rapidly amplify the ambient Alfvén waves, by several orders of magnitude in the inner heliosphere. Energetic minor ions find themselves traveling through resonant Alfvén waves previously amplified by higher velocity protons. The nonuniformly growing wave spectra alter the rigidity dependence of particle scattering, resulting in complex time variations of SEP abundances at large distances from the Sun. The greatly amplified waves travel outward in an expanding and weakening "shell," creating an expanding and falling "reservoir" of SEPs with flat spatial intensity profiles behind, while in and beyond the shell the intensities drop steeply. The wave-particle resonance relation dynamically links the evolving characteristics of the SEP and Alfvén wave distributions in this new mode of SEP transport. We conclude that wave amplification, the counterpart to the scattering of streaming particles required by energy conservation, plays an essential role in the transport of SEPs in gradual SEP events. The steep proton-amplified wave spectra just upstream of the shock suggest that they may also be important in determining the elemental abundances of shock-accelerated SEP sources.

Subject headings: acceleration of particles — interplanetary medium — solar wind — Sun: particle emission — waves

1. INTRODUCTION

A large body of observational evidence suggests that energetic charged particles detected by instruments aboard spacecraft and on the ground in gradual solar energetic particle (SEP) events are accelerated at shock waves driven by fast coronal mass ejections (CMEs) from the Sun (Kahler 2001; Tylka 2001; Lee 1997, 2000; Reames 1997, 1999; Ryan, Lockwood, & Debrunner 2000; Lee & Ryan 1986; Kahler et al. 1984; Cane, Reames, & von Rosenvinge 1988; Reames, Barbier, & Ng 1996). Because of the great complexity of the phenomenon, a rigorous comprehensive theory of the shock acceleration and transport of SEPs does not exist. Nevertheless, shock acceleration of protons to $\gtrsim 1$ GeV close to the Sun is expected on general theoretical grounds (Lee 1997). Early analytical work on the steady state acceleration of SEPs at coronal shocks was made by Achterberg & Norman (1980) and Lee & Fisk (1982). Lee & Ryan (1986) modeled analytically time-dependent test-particle diffusive shock acceleration at a spherical solar blast wave, showing that protons can be accelerated from 0.5 MeV to 1 GeV in $\sim$2 hr. In the numerical model of Zank, Rice, & Wu (2000) assuming Bohm diffusion, SEPs are accelerated to greater than 1 GeV early in the event at an evolving CME-driven shock starting out at 20 $R_\odot$ (Rice & Zank 2000).

For SEPs to gain energy quickly via the first-order Fermi mechanism (e.g., Axford, Leer, & Skadron 1977), intense plasma waves must exist so that particles can be scattered

[1] Also Department of Astronomy, University of Maryland, College Park, MD 20742.

rapidly back and forth across the shock. Observations of impulsive SEP events suggest that the particle mean free paths λ are often $\gtrsim 0.5$ AU in interplanetary (IP) space (e.g., Mason et al. 1989). What then is the origin of these high-intensity waves? It has been suggested that wave amplification by the SEPs themselves is the answer (e.g., Bell 1978) since wave-particle interaction predicts in one self-consistent package both particle scattering by waves and concomitant wave amplification by streaming particles (e.g., Lee 1971). Steady state planar models of particle acceleration coupled self-consistently to quasilinear wave excitation were put forward by Bell (1978) for astrophysical shocks, by Achterberg & Norman (1980) for flare-generated coronal shocks, and by Lee (1982, 1983) for planetary bow shocks and traveling IP shocks. In fact, "self-amplified" waves were invoked many decades ago to explain the confinement of cosmic rays in the Galaxy (Wentzel 1974). However, for the IP medium, theoretical and observational studies of the impact of self-amplified waves on SEPs and IP energetic ions have been comparatively recent. Many predictions of the Lee (1983) model on shock-accelerated ions and resonant waves were confirmed by in situ observations of $\lesssim 100$ keV amu^{-1} particles and resonant waves in a number of IP shock events (Viñas, Goldstein, & Acuña 1984; Tsurutani, Smith, & Jones 1983; Sanderson et al. 1985; Tan et al. 1989; Kennel et al. 1986; Gordon et al. 1999). These confirmations suggest that the predictions of models based on quasilinear theory (QLT) are valid at higher energies for stronger shocks closer to the Sun (Lee 1997).

For low-energy ($\lesssim 0.2$ MeV amu^{-1}) SEPs, shock acceleration efficiency often remains strong as the shock propagates from the Sun to beyond 1 AU. For high-energy ($\gtrsim 10$ MeV amu^{-1}) SEPs, however, it usually diminishes very quickly with heliocentric distance (e.g., Zank et al. 2000), as does resonant wave amplification (Ng & Reames 1994; Ng, Reames, & Tylka 1999a, 1999b). Therefore, in contrast to low-energy ions, for which the observed particle and resonant wave intensities both peak near the time of shock passage, the high-energy SEPs often reach maximum intensities when the shock and the greatly amplified waves are still near the Sun.[2] These distant amplified Alfvén waves cannot be remotely sensed, but they leave telltale observable imprints on the SEPs in a number of important, interesting ways.

One such observational characteristic is the apparent limit in the *early* SEP intensities at 1 AU (Reames & Ng 1998). Another is the time variations of SEP elemental abundances. The 1998 April 20 gradual event is an interesting example (Tylka, Reames, & Ng 1999). At ~ 3.7 MeV amu^{-1}, the abundance ratios of Fe, S, Si, Ne, and C relative to O showed complex but systematic time variation, ordered by A/Q, the mass-to-charge ratio. However, the He/H ratio evolved in a manner apparently contrary to the A/Q ordering expected from QLT, rising when Fe/O was falling, and falling when the latter was rising (see also Witte et al. 1979; Mason, Gloeckler, & Hovestadt 1983). In a comparison of large versus small and hard versus soft gradual SEP events, Reames, Ng, & Tylka (2000) found that the former tend to be observed with He/H ratio initially rising from less than coronal and the latter with He/H falling from greater than coronal. There is also a tendency for observed particle anisotropies to be smaller for larger gradual events (Reames, Ng, & Berdichevsky 2001).

The above observed features are very difficult, if not impossible, to understand without wave amplification. The complex time variations of SEP abundance ratios cannot be explained using time-independent transport parameters in the classical diffusion, diffusion convection, or focused transport models. One would have to abandon the observed rigidity dependence of ion scattering as predicted by QLT (Jokipii 1966; Hasselmann & Wibberenz 1968; Schlickeiser 1989a) or dynamical turbulence theory (Bieber et al. 1994) for Kolmogorov or Kraichnan spectrum of waves or turbulence and invoke arbitrary and drastically different transport parameters and/or time injection functions, even for two ion species with A/Q values differing by less than a factor of $\lesssim 2$ (see Appendix C on the classical diffusion model). In contrast, self-consistent quasilinear wave amplification is required by both the physics of wave-particle interaction (e.g., Lee 1971, 1982) and energy conservation (see Appendix B). It is therefore a natural candidate to consider in attempting to understand the observations.

Using a time-dependent numerical model that incorporates magnetic focusing, pitch-angle diffusion, and quasilinear wave growth, Ng & Reames (1994) showed that energetic protons streaming from a fixed solar source amplify preexisting IP Alfvén waves by orders of magnitude. In turn, the amplified waves near the Sun limit the early proton intensity at 1 AU, in general agreement with the observation (Reames & Ng 1998). By modifying the above model to include a moving source of shock-accelerated multispecies ions, the time variation of the abundance ratios relative to oxygen, as well as of He/H in the 1998 April 20 event, was reproduced semiquantitatively (Ng et al. 1999a, 1999b; Tylka 2001). In particular, it was demonstrated that the observed initial rise of the He/H ratio (normalized to coronal values) from less than 1 was due to enhanced scattering of helium ions by waves resonantly amplified by faster protons with twice or greater velocity. For simplicity, the above models ignored solar wind convection and adiabatic deceleration, as well as wave transport.

It is our purpose in this paper to present a model that takes account of various known relevant physical processes and has the potential to explain qualitatively and perhaps quantitatively the observed features mentioned above. The processes included are magnetic focusing by the interplanetary magnetic field (IMF), solar wind convection, adiabatic deceleration, and resonant pitch-angle scattering by IP Alfvén waves for particles and WKB transport and wave growth by the same QLT that gives pitch-angle scattering for waves. It also incorporates shock acceleration via a moving SEP source term that depends on plasma and shock parameters. This model is more general than the ones in Ng et al. (1999a, 1999b) in including solar wind convection, adiabatic deceleration, WKB wave transport, and a more considered SEP source term, as well as covering wider energy and wavenumber ranges.

A preliminary report has been given of the successful fit of this model to the concurrent time histories and evolving energy spectra of the absolute intensities of proton, He, O, and Fe ions, as well as concurrent He/H and Fe/O ratios in the 1998 September 30 and 2000 April 4 gradual SEP events (Ng, Reames, & Tylka 2001). In addition, a successful preliminary explanation of unusual angular distribution of Fe/O has been given (Reames & Ng 2002).

[2] However, there have been events, e.g., 1989 October 20 and 2001 November 5, in which ~ 500 MeV protons peak near shock crossing.

In the following, we present a detailed description of the model (§ 2), its numerical solution (§ 3), and representative results on various aspects of the coupled SEPs and Alfvén waves, with careful interpretations linking the simultaneously evolving particle and wave distributions through gyroresonant interaction, and with particular emphasis on SEP abundance variation (§ 4). We will demonstrate clearly the twin roles of wave-particle interaction: particle scattering and wave amplification. Combined with solar wind convection, they give a new mode of SEP transport with interesting implications on gradual SEP events. We also show in § 4 how a disturbed region beyond 1 AU influences differently the anisotropies of different species of SEPs at 1 AU. In § 5 we close the paper with a summary and discussion.

2. THE MODEL

2.1. *Scenario and Assumptions*

We envisage the following scenario. A CME is launched from the Sun, driving a shock in the high corona. The shock propagates outward and accelerates suprathermal ions in the ambient plasma to high energies. As the accelerated ions stream away from the shock, they excite plasma waves that pitch-angle scatter the ions, thereby enhancing the shock's efficiency to accelerate them to still higher energies via the first-order Fermi mechanism. As shock acceleration proceeds, some energetic ions escape and travel away from the shock. As the ions stream outward through the IP medium, they amplify the ambient resonant plasma waves, simultaneously undergoing pitch-angle scattering by these waves; they are focused by the diverging IMF and experience convection and adiabatic deceleration in the expanding solar wind. An SEP event is observed when some of these particles propagate to a distant spacecraft. The shock may also accelerate electrons (Mann, Classen, & Motschmann 2001; Potter 1981). However, the details of electron acceleration and transport are different from those in the acceleration of ions. In this paper we consider only energetic ions.

The acceleration and transport of SEPs in gradual events are complex processes in a rapidly evolving inhomogeneous medium. The great complexity precludes a rigorous treatment encompassing particle acceleration and transport, as well as the evolution of shock and IP waves (Lee 1997; Lee & Ryan 1986). In this paper we employ an idealized model incorporating quasilinear wave-particle interaction to explore the consequences of coupling IP Alfvén waves to SEPs. We are interested in the concurrent evolution of the multispecies gyrophase-averaged phase-space densities $f_s(\mu, P, r, t)$ of s-species energetic ions and the spectral magnetic intensities $I^{\sigma}(k, r, t)$ of σ-mode Alfvén waves.[3] The model generalizes those reported in Ng & Reames (1994) and Ng et al. (1999a, 1999b). Through model simulations, we study how the SEP intensity spectra, elemental abundances, and anisotropies, as well as the Alfvén wave spectra and associated particle mean free paths, evolve in space and time in response to wave growth and also how the evolution depends on the parameters characterizing the IP medium, shock, and energetic ion sources.

[3] The other symbols are explained in connection with eqs. (5) and (6).

Several simplifications are necessary to render the model tractable. The result is an idealized model that incorporates salient features of the physical processes at work. We assume that the shock accelerates ions in the high corona ($r \gtrsim 3\ R_{\odot}$) where collisional ionization is negligible (Ruffolo 1997), although some shocks may start lower down in denser solar atmosphere, leading to possibly significant charge stripping of the SEPs during acceleration (Barghouty & Mewaldt 2000; Reames, Ng, & Tylka 1999; Ostryakov et al. 2000).

The SEPs interact with a variety of plasma waves in the IP medium, but for simplicity we consider only parallel propagating Alfvén waves. Because SEP acceleration is rapid compared to their IP transport (at least early in the event), we decouple acceleration from transport by injecting prescribed spectra of energetic ion populations at a traveling shock. It is customary to neglect cross field transport and treat SEP transport along corotating Parker spiral IMF. However, evolving Alfvén waves propagating across the spiral IMF make the model fully dependent on heliographic longitude and latitude. This increase in dimension renders the model intractable, requiring treatment of wave propagation beyond the scope of this paper. We therefore eschew realism for simplicity and assume a radial IMF, allowing WKB treatment of wave propagation parallel to the IMF in the moving IP medium.

For SEP transport, the model includes the effects of particle motion, magnetic focusing, solar wind convection with adiabatic deceleration, and resonant pitch-angle scattering by Alfvén waves (Jokipii 1966; Schlickeiser 1989a, 1989b). An extended QLT (Ng & Reames 1995) is used so that the particles are able to diffuse across 90° pitch angle through resonance broadening (Bieber et al. 1994; Schlickeiser & Achatz 1993a, 1993b). We ignore particle momentum transport required by QLT, as it proceeds slower than pitch-angle diffusion by $O(V_{\rm A}/v)$. In the model, a spherical "shock" propagates with prescribed velocity $V_{\rm sh}$ into a solar wind, which travels radially outward with constant radial velocity $V_{\rm sw}$. For our purpose, the shock serves only as a traveling source of SEPs, and plasma velocity jump across it is ignored. The model thus underestimates convection and adiabatic deceleration in the downstream region with, however, relatively minor effects in our simulations, since our focus is on the evolution of SEPs and waves upstream of the shock. Plasma velocity jump will be included in future models. The injection spectra are power laws in rigidity taken from the steady state model of shock acceleration (e.g., Lee 1983), with the same seed particle velocity for all ion species and with the following modifications. The power-law spectral index is time-dependent to allow for an evolving shock compression ratio. Acceleration limit due to finite shock lifetime and/or particle escape from the shock is accounted crudely by steepening the ion spectra with an exponential factor, in which the e-folding energy per amu constant $E_e Q_s/A_s$ of s-ions varies inversely with the shock radius (Zank et al. 2000) and is proportional to Q_s/A_s (Ellison & Ramaty 1985; Tylka et al. 2000), where Q_s is the ionic charge in units of elementary charge e and A_s is the atomic mass.

Upstream of the shock, streaming SEPs rapidly amplify outward (antisunward) and damp inward (sunward) Alfvén waves by orders of magnitude. As the amplified upstream waves cross the advancing shock to downstream, they undergo partial mode conversion, their

wavenumbers increase, and they are further amplified (Webb et al. 1999). For a parallel shock, Vainio & Schlickeiser (1999) calculated the cross shock wave amplification at constant wavenumber to be greater than 10. On the other hand, in the downstream region, SEPs streaming inward from the shock will damp outward waves and amplify mode-converted inward waves, although the IMF tends to mirror these SEPs and reduce the effect. Rather than simulate the above complex processes, we simplify the downstream situation as follows. We consider only outward right-hand ($\sigma = R^+$) and outward left-hand ($\sigma = L^+$) circularly polarized Alfvén waves. Upstream, these waves are coupled to the energetic protons and He^{+2} ions. Downstream, the SEP-driven wave growth rate is set to zero, in a conceptual trade-off between cross shock amplification of outward waves and SEP amplification of inward waves on the one hand and SEP damping of outward waves on the other. Thus, the amplified upstream waves continue to scatter SEPs downstream, analogous to the downstream convective approximation in classical shock acceleration models (e.g., Lee 1983). In another version of this model that included both outward and inward Alfvén waves, we found that in the downstream region inward wave amplification roughly compensates for outward wave damping.

The initial IP Alfvén wave distributions are specified as steady state WKB solutions to the wave kinetic equation for solar sources with Kolmogorov spectra, subject to a small phenomenological wave energy damping rate, typically $\sim$0.01 hr^{-1} (Ng & Reames 1994; Bavassano et al. 1982). These initial wave distributions have Kolmogorov spectra everywhere, a convenient initial state from which to assess subsequent SEP-driven wave growth and associated effects. Initially, the IP medium is taken to be empty of SEPs. Then energetic protons and ions are injected at a moving "shock." The subsequent evolution of the wave and particle distributions is obtained by solving the initial boundary value problem described below.

2.2. *Governing Equations*

2.2.1. *Energetic Particle Transport*

We assume a constant radial solar wind with speed V_{sw} and a radial mean interplanetary magnetic field. The magnetic induction B, the solar wind s-ion number density n_s, and the Alfvén speed V_A are given, respectively, by

$$B(r) = B_0\left(\frac{r_0}{r}\right)^2 , \quad (1)$$

$$n_s(r) = n_{s,0}\left(\frac{r_0}{r}\right)^2 , \quad (2)$$

$$V_A(r) = V_{A,0}\frac{r_0}{r} , \quad (3)$$

where B_0, $n_{s,0}$, and $V_{A,0}$ are the respective values at $r_0 = 1$ AU. Note that

$$V_{A,0} = B_0\left(4\pi m_p n_{H,0}\right)^{-1/2} , \quad (4)$$

where m_p is the proton mass. On a radial magnetic flux tube, the evolution of the phase-space densities $f_s(\mu, P, r, t)$ of s-species energetic ions is governed by the particle transport equation (Skilling 1975; Ruffolo 1995; see also other references cited in this paragraph)

$$\frac{\partial f_s}{\partial t} + (\mu v + V_{sw})\frac{\partial f_s}{\partial r} + \frac{1-\mu^2}{r}(v + \mu V_{sw})\frac{\partial f_s}{\partial \mu} - \frac{1-\mu^2}{r}V_{sw}P\frac{\partial f_s}{\partial P} - \frac{\partial}{\partial \mu}\left(D_{\mu\mu}\frac{\partial f_s}{\partial \mu}\right) = g_s , \quad (5)$$

where t is time, r is heliocentric distance, v is particle velocity, P is rigidity, μ is pitch-angle cosine, and V_{sw} is constant solar wind velocity. "Mixed" coordinates are used: r, t in the fixed frame and v, P, μ in the solar wind frame. Equation (5) is a statement of the conservation of particles. The second through the last terms in the equation are due to particle motion parallel to the IMF, magnetic focusing in the diverging IMF, adiabatic deceleration in the expanding solar wind plasma, resonant pitch-angle scattering by Alfvén waves (Hasselmann & Wibberenz 1968; Jokipii 1966), and shock-accelerated ion source, respectively. The influence of the solar wind is manifest through the presence of V_{sw} in the second, third, and fourth terms. We have ignored in equation (5) the following: terms of $O(vV_{sw}/c^2)$ and time-varying magnetic field (Kulsrud & Pearce 1969), the spiral Parker IMF and variable solar wind velocity (Skilling 1975; Ruffolo 1995; Isenberg 1997; Lu, Zank, & Webb 2001), and particle momentum transport associated with the tensor elements $D_{\mu P}$ and D_{PP} (Schlickeiser 1989a, 1989b), which are smaller than the pitch-cosine diffusion coefficient $D_{\mu\mu}$ by $O(V_A/v)$ and $O[(V_A/v)^2]$, respectively (Appendix B). Equation (5) reduces to the focused transport equation (Kulsrud & Pearce 1969; Roelof 1969) for $V_{sw} = 0$.

The diffusion coefficient $D_{\mu\mu}$ in the solar wind frame is related to the Alfvén wave spectral magnetic intensities I^σ as follows:

$$D_{\mu\mu}(\mu, v, P, r, t) = \sum_\sigma \frac{v^2}{4P^2}\int dk\, I^\sigma(k, r, t) R^\sigma_{\mu\mu}(\mu, v, P, k, V_\sigma, B) , \quad (6)$$

where the sum is over all Alfvén wave modes, $V_\sigma = \pm V_A$ is the wave velocity in the plasma frame, and $R^\sigma_{\mu\mu}$ is the wave-particle resonance function. Note that $D_{\mu\mu}$ depends on both v and P, i.e., v and A/Q, since $P = Am_pc\gamma v/Qe$, where m_p is the proton mass and γ is the Lorentz factor. At constant P, its dependence on v or A/Q is weak, except when $v \sim V_A$.

To evaluate $D_{\mu\mu}$ from $I^\sigma(k, r, t)$, we adopt for $R^\sigma_{\mu\mu}$ a closed form approximation (Appendix A, eq. [A1]) to the "broadened" resonance function of Ng & Reames (1995; see also Bieber et al. 1994; Schlickeiser & Achatz 1993a, 1993b). For $|\mu| \gtrsim 0.7$, this $R^\sigma_{\mu\mu}$ gives a narrow resonance close to the prediction of the standard quasilinear theory (Jokipii 1966; Hasselmann & Wibberenz 1968). For $|\mu| \lesssim 0.3$, however, it gives a much broader resonance, allowing the particles to interact with hydromagnetic Alfvén waves and bridge the quasilinear resonance gap extending across $\mu = 0$. The standard quasilinear theory gives

$$R^\sigma_{\mu\mu} = \left(1-\mu^2\right)\left(1 - \frac{\mu V_\sigma}{v}\right)^2 2\pi\delta\left(k\mu v - kV_\sigma - \frac{\Omega}{\gamma}\right) , \quad (7)$$

where $\Omega = QeB/(Am_pc)$ is the ion cyclotron frequency. This sharp resonance results in a resonance gap for a wave spectrum that steepens at high wavenumbers as a result of, e.g.,

thermal damping, or that has a high wavenumber cutoff such as imposed in a numerical model.

2.2.2. *Moving Source of Shock-accelerated Ions*

The injection of $\sim$1 GeV protons soon after CME initiation (Kahler 1994) suggests that acceleration is very rapid compared to IP transport and that we may decouple acceleration from transport early in an SEP event. If the shock weakens after traveling many tenths of AU, the acceleration and transport timescales may become comparable. A time-dependent model that treats self-consistently SEP shock acceleration and transport together with IP Alfvén wave amplification and transport is, however, beyond our scope. For simplicity, we decouple acceleration and transport and inject at time $t \gtrsim 0$ isotropic distributions of accelerated s-ions at the traveling shock via the source term:

$$g_s(r, P, t) = \frac{bn_s(r)(V_{\rm sh} - V_{\rm sw})(\alpha - 3)}{4\pi P_{0,s}^3} \times \left(\frac{P}{P_{0,s}}\right)^{-\alpha} \exp\left[-\frac{evP}{2cE_e(r)}\right] \delta(r - r_{\rm sh}) \ . \quad (8)$$

It is assumed the shock travels outward from $r = r_{\rm sh,0}$ with prescribed shock velocity $V_{\rm sh}(t)$. At time t, it is at

$$r_{\rm sh}(t) = r_{\rm sh,0} + \int_0^t V_{\rm sh}(t')dt' \ . \quad (9)$$

The Dirac δ-function in equation (8) localizes the ion sources at $r_{\rm sh}(t)$; i.e., their scale lengths are assumed $\ll \Delta r$, the computational grid size. We assume that the energetic source ions are accelerated out of the suprathermal tail and take g_s to be proportional to $n_s(V_{\rm sh} - V_{\rm sw})$, the solar wind s-ion flux into the shock. Because the observed velocity distributions of solar wind ions are very similar (Ogilvie et al. 1993), we assume identical seed velocity v_0 (or identical seed energy per amu $E_{0,s}/A_s$) for all species, implying injection rigidities

$$P_{0,s} = \left(\frac{A_s}{Q_s}\right)\left(\frac{m_p c}{e}\right) v_0 = \left(\frac{A_s}{Q_s}\right)\left(\frac{2E_{0,s}m_p c^2}{A_s e^2}\right)^{1/2} . \quad (10)$$

All ion source spectra follow the same rigidity power law at low rigidities (eq. [8]). This is motivated by the shock spectra predicted by steady state acceleration models (e.g., Lee 1983), spectral variation upstream of the shock being ignored. The steady state models give the power-law spectral index $\alpha = 3c_r/(c_r - 1)$, with c_r the shock compression ratio. However, to allow for an evolving compression ratio, it is more convenient to specify α directly, e.g.,

$$\alpha(r_{\rm sh}) = \alpha_0 + \alpha'(r_{\rm sh} - r_{\rm sh,0}) \ , \quad (11)$$

with α_0 the initial spectral index and $\alpha' = d\alpha/dr_{\rm sh}$.

The exponential factor in the source terms (eq. [8]) differentially steepens the s-ion source spectra at energies per amu $E/A_s \gtrsim E_e^s/A_s \equiv E_e Q_s/A_s$, assumed nonrelativistic. Note that $evP/(2c) = \gamma(A_s/Q_s)\frac{1}{2}m_p v^2$ for s-ions. This is motivated by the observed SEP spectral "knee" at high rigidities (Ellison & Ramaty 1985; Tylka et al. 2000; Tylka 2001). It is believed that finite shock lifetime (Forman & Webb 1985) and/or particle escape from a shock of finite spatial extent (Eichler 1981; Lee 1982) impose a limit on particle acceleration, leading to the spectral steepening. We assume

$$E_e(r_{\rm sh}) = \frac{E_{e,0}r_{\rm sh,0}}{r_{\rm sh}} \ , \quad (12)$$

in analogy to the radial dependence of the maximum particle energy in the shock acceleration model of Zank et al. (2000). If $E_e \gg evP_{0,s}/2c$, the total number of s-ions injected per (cm^2 hr) is $\int_{P_{0,s}}^{\infty} 4\pi P^2 \int g_s \, dr \, dP \approx bn_{s,0}(V_{\rm sh} - V_{\rm sw})$, so that b represents the seed particle fraction of the solar wind s-ion flux. This clearly requires $b \ll 1$. However, this should not be taken literally because the true source spectrum may not follow an extrapolated power law down to $P_{0,s}$. The physical parameters in the source terms given by equation (8) determine their temporal, spatial, and spectral characteristics and thereby the model predictions. Note that the assumed decrease of n_s and E_e with $r_{\rm sh}(t)$ and a positive α' all imply that the source term g_s decays quickly in time. This may be a factor in the systematic discrepancies between solar wind and SEP composition (e.g., Mewaldt et al. 2001).

2.2.3. *Alfvén Wave Transport*

We start with the wave kinetic equation (Stix 1992; Barnes 1992; Dewar 1970) for the conservation of wave action in a frame fixed relative to the Sun:

$$\frac{\partial \mathcal{N}_\sigma}{\partial t} + \frac{\partial \omega}{\partial \boldsymbol{k}} \cdot \frac{\partial \mathcal{N}_\sigma}{\partial \boldsymbol{r}} - \frac{\partial \omega}{\partial \boldsymbol{r}} \cdot \frac{\partial \mathcal{N}_\sigma}{\partial \boldsymbol{k}} = \gamma_\sigma \mathcal{N}_\sigma \ , \quad (13)$$

where $\mathcal{N}_\sigma$ is the wave action density, ω is the wave angular frequency, $\boldsymbol{k}$ is the wave vector, $\boldsymbol{r}$ is the position vector, and $\gamma_\sigma \mathcal{N}_\sigma$ is a source term. Assuming radially outward propagating waves, the wave action density $\mathcal{N}_\sigma$ may be written as

$$\mathcal{N}_\sigma(\boldsymbol{k}, \boldsymbol{r}, t) = \frac{N_\sigma(k, r, t)}{k^2 \sin\theta_k} \delta(\theta_k - \theta)\delta(\phi_k - \phi) \ , \quad (14)$$

where (r, θ, ϕ) are the spatial spherical coordinates and (k, θ_k, ϕ_k) are the spherical coordinates in $\boldsymbol{k}$-space with the polar axis aligned along $\boldsymbol{r}$. For time-independent wave dispersion relation in the fixed reference frame,

$$\omega = kV_{\sigma f} = k(V_{\rm sw} + V_\sigma) = k(V_{\rm sw} + V_{\rm A}) \ , \quad (15)$$

we have $d\omega/dt = \partial\omega/\partial t = 0$. Using this time independence and the relation

$$\omega N_\sigma \propto \frac{2V_{\sigma f} I^\sigma}{V_\sigma} \ , \quad (16)$$

we may derive from equations (13), (14), and (15) the evolution equation for the spectral magnetic intensity $I^\sigma(k, r, t)$ of the outward Alfvén waves ($V_\sigma = V_{\rm A}$):

$$\frac{\partial}{\partial t}\left(\frac{V_{\sigma f}}{V_\sigma} I^\sigma\right) + \frac{1}{r^2}\frac{\partial}{\partial r}\left(r^2 \frac{V_{\sigma f}^2}{V_\sigma} I^\sigma\right) - \frac{\partial}{\partial k}\left(k \frac{dV_{\sigma f}}{dr}\frac{V_{\sigma f}}{V_\sigma} I^\sigma\right) = \gamma_\sigma \frac{V_{\sigma f}}{V_\sigma} I^\sigma \ . \quad (17)$$

The Alfvén wave spectral magnetic intensities $I^\sigma(k, r, t)$ are normalized such that

$$\langle \delta\boldsymbol{B} \cdot \delta\boldsymbol{B} \rangle = \sum_\sigma \int_0^\infty dk I_\sigma(k, r, t) \ , \quad (18)$$

where $\delta\boldsymbol{B}$ is the magnetic field fluctuation due to Alfvén waves and angle brackets denote ensemble average.

2.2.4. *Wave Growth Rate*

The right-hand sides of equations (13) and (17) are due to wave sources/sinks. The net growth rate γ_σ of I^σ is specified as follows:

$$\gamma_\sigma(k,r,t) = 2\pi^2 c V_\sigma \sum_s Q_s^3 e^3 \iint d\mu\, dP \frac{P^3}{\mathscr{E}^2} \frac{R^\sigma_{\mu\mu}}{(1-\mu V_\sigma/v)^2} \times \left[\frac{\partial f_s}{\partial \mu} - \frac{V_\sigma}{v}\left(\mu \frac{\partial f_s}{\partial \mu} - P\frac{\partial f_s}{\partial P}\right)\right] + \zeta \,. \quad (19)$$

Here $\mathscr{E} = A\gamma m_p c^2$ is the total particle energy, with γ the Lorentz factor. The first term in equation (19) is the wave energy growth rate driven by the momentum gradients of the plasma-frame ion phase-space densities f_s. We give its derivation from the conservation of the total energy of waves and particles in quasilinear interaction in Appendix B. For a derivation from the plasma dispersion relation, see, e.g., Lee (1971, 1982) or Melrose (1980). The energetic protons dominate the sum by far. In calculating γ_σ, we neglect all minor ions except He^{+2}, which constitute $\sim$3.6% of the solar wind number density. Not unexpectedly, the He^{+2} contribution turns out to be negligible (e.g., Lee 1983). In terms of $f_{v,s}$, the ion density in $(\boldsymbol{r},\boldsymbol{v})$-space, the s-ion contribution scales roughly as $(Q_s^2/A_s)(\partial f_{v,s}/\partial\mu)$. The second term ζ on the right-hand side of equation (19) represents the wave energy change rate due to additional processes yet to be specified. For the cases reported in this paper, we specify $\zeta = \zeta_1 = -0.01\ \mathrm{hr}^{-1}$ as a small phenomenological damping rate (Bavassano et al. 1982), which preserves a power-law wave spectrum when used in equation (17) in the absence of other driving terms.

2.2.5. *Coupled Equations in Conservative Form*

For numerical solution it is preferable to express the particle transport equation and the wave kinetic equation in conservative form. To this end, we multiply the particle transport equation (5) by $B_0P^3/BP_{0,s}^3$ and transform it into

$$\frac{\partial F_s}{\partial t} + \frac{\partial}{\partial r}[(\mu v + V_{\rm sw})F_s] + \frac{\partial}{\partial \mu}\left[\frac{1-\mu^2}{r}(v+\mu V_{\rm sw})F_s\right] - P\frac{\partial}{\partial P}\left(\frac{1-\mu^2}{r}V_{\rm sw}F_s\right) - \frac{\partial}{\partial\mu}\left(D_{\mu\mu}\frac{\partial F_s}{\partial\mu}\right) = G_s \,, \quad (20)$$

a particle transport equation governing the modified ion phase-space densities

$$F_s(\mu,P,r,t) = f_s(\mu,P,r,t)\frac{B_0}{B}\frac{P^3}{P_{0,s}^3} = f_s(\mu,P,r,t)\frac{r^2}{r_0^2}\frac{P^3}{P_{0,s}^3} \,, \quad (21)$$

with the modified ion source terms

$$G_s = \frac{bn_{s,0}(V_{\rm sh}-V_{\rm sw})(\alpha-3)}{4\pi P_{0,s}^3}\left(\frac{P}{P_{0,s}}\right)^{3-\alpha} \times \exp\left(-\frac{evP}{2cE_e}\right)\delta(r-r_{\rm sh}) \,. \quad (22)$$

Note the replacement of $n_s(r)$ in equation (8) by the constant $n_{s,0}$ in equation (22). Similarly, the wave evolution equation (17) may be transformed into the conservative form

$$\frac{\partial \Psi_\sigma}{\partial t} + \frac{\partial}{\partial r}(V_{\sigma f}\Psi_\sigma) + \eta\frac{\partial}{\partial\eta}\left[\left(2\frac{V_{\sigma f}}{r} - \frac{dV_{\sigma f}}{dr}\right)\Psi_\sigma\right] = \gamma_\sigma\Psi_\sigma \,, \quad (23)$$

governing the modified spectral wave intensity

$$\Psi_\sigma(\eta,r,t) = 2I^\sigma(k,r,t)\frac{V_{\sigma f}kB_0}{V_\sigma k_0 B} \,. \quad (24)$$

In equations (23) and (24), we use the modified wavenumber $\eta = k/B$ in place of the wavenumber k as an independent variable to facilitate interpretation in the framework of wave-particle resonant interaction, which relates k/B in MV^{-1} and μP in MV by

$$\frac{k}{B} = \left[\left(\mu - \frac{V_{\rm A}}{v}\right)P\right]^{-1} \approx (\mu P)^{-1} \,. \quad (25)$$

In terms of F_s and Ψ_σ, $D_{\mu\mu}$ (eq. [6]) and γ_σ (eq. [19]) are, respectively,

$$D_{\mu\mu}(\mu,P,r,t) = \sum_\sigma \int d\eta \frac{v^2}{8P^2}\frac{V_\sigma}{V_{\sigma f}}\frac{\eta_0}{\eta} \times B\Psi_\sigma(\eta,r,t)R^\sigma_{\mu\mu}(\mu,v,P,\eta,V_\sigma,B) \,, \quad (26)$$

$$\gamma_\sigma(\eta,r,t) = 2\pi^2 c V_\sigma \sum_s Q_s^3 e^3 \iint d\mu\, dP \frac{P_{0,s}^3}{\mathscr{E}^2}\frac{B}{B_0}\frac{R^\sigma_{\mu\mu}}{(1-\mu V_\sigma/v)^2} \times \left\{\frac{\partial F_s}{\partial\mu} - \frac{V_\sigma}{v}\left(\mu\frac{\partial F_s}{\partial\mu} - P\frac{\partial F_s}{\partial P} + 3F_s\right)\right\} + \zeta \,. \quad (27)$$

The evolution equations (20) and (23) for $F_s(\mu,P,r,t)$ and $\Psi_\sigma(\eta,r,t)$, respectively, are coupled together via equation (26) expressing $D_{\mu\mu}(\mu,v,P,r,t)$ in terms of $\Psi_\sigma(\eta,r,t)$ and equation (27) giving $\gamma_\sigma(\eta,r,t)$ in terms of $F_s(\mu,P,r,t)$. To simulate a gradual SEP event, we solve the initial boundary value problem defined by the coupled equations (20) and (23) subject to appropriate initial and boundary conditions.

2.3. *Initial and Boundary Conditions*

2.3.1. *Domains of the SEP and Alfvén Wave Distributions*

While the μ range is clearly $[-1, 1]$, the choice of r, P, and η boundaries requires some discussion. The lower spatial boundary r_a should ideally be placed where the shock begins to accelerate the SEPs, probably at r equal to several $R_\odot$. However, at $r \lesssim 10\ R_\odot$, the magnetic field, plasma density, and Alfvén speed cannot be approximated by the simple forms in equations (1)–(3). We adopt the compromise $r_a = 0.05\ \mathrm{AU} = 11.34\ R_\odot$.

There is some evidence from SEP observations that the particles may be quasi-trapped inside a region bordered by increased scattering and/or increased magnetic field associated with IP shocks at $r \gtrsim 1.5$ AU (Bieber et al. 2002; Reames & Ng 2002) or inside a magnetic bottle associated with a previous CME (Reames 2002). We approximate the influence of such constraints with a partially reflecting *moving* outer boundary at $r_b(t)$ (see eq. [35]). The initial boundary location $r_{b,0}$ is arbitrary, but note that the

assumed radial IMF deviates significantly from the Parker field at $r \gtrsim 1$ AU.

We next consider the related P and η ranges. Say we are interested in ions with A/Q from 1 to $\sim$5 in the P range (10, 1900) MV (e.g., 60 keV to 1.2 GeV protons, 330 keV amu^{-1} to 110 MeV amu^{-1} Fe^{+14} ions). According to QLT, the resonant η is given by $\eta_{\rm res} \approx (|\mu|P)^{-1}$ and the resonant P by $P_{\rm res} \approx (|\mu|\eta)^{-1}$. With $-1 \lesssim \mu \lesssim 1$, this implies that ions in the above P range resonate with waves in the η range $(5.26 \times 10^{-4}, \infty)$ MV^{-1}. These waves in turn resonate with ions in the P range (0, 1900) MV. However, we really only require a finite η range, and so the P range need not extend below 10 MV. This is because of strong wave damping at high frequency through thermal and other dissipations, as well as resonance broadening. The damping rate increases steeply as a function of $kV_{\rm A}/\Omega_p$ (Gary 1993; Leamon et al. 1998), steepening the wave spectrum at high η and resulting in a quasilinear resonance gap around $\mu = 0$. This resonance gap is, however, artificial: resonance broadening allows ions at $|\mu| \lesssim 0.3$ to interact with hydromagnetic waves at η much less than $(|\mu|P)^{-1}$ (Bieber et al. 1994; Schlickeiser & Achatz 1993a, 1993b; Ng & Reames 1995). In the near-Sun region, the damping limits the intensity of high-frequency hydromagnetic waves that would otherwise be amplified to extremely high levels by streaming low-rigidity protons. This damping may be heuristically treated via the ζ term in the expression for γ_σ (eq. [19]). It also suggests that we specify an upper cutoff wavenumber η_c below the range of ion-cyclotron waves, say,

$$\eta_c = \frac{c_d \Omega_p}{BV_{\rm A}} = \frac{c_d ec}{m_p c^2 V_{\rm A}} \ , \tag{28}$$

with the constant $c_d \lesssim \frac{1}{2}$. A more graceful way is to extend the wave spectrum beyond η_c with an η^{-4} spectrum. With $V_{\rm A}$ from equation (3), $c_d = \frac{1}{2}$, $m_p c^2 = 938$ MeV, and $c = 7.2$ AU hr^{-1}, we have

$$\eta_c = \frac{3.83 \times 10^{-3} \text{ AU hr}^{-1}}{V_{\rm A,0}} \frac{r}{r_0} \text{ MV}^{-1} \ . \tag{29}$$

As the waves propagate to larger r, their η increases (see § 2.2.3) faster than η_c given in equation (28) or equation (29). For $V_{\rm A,0} \simeq 1 \times 10^{-3}$ AU hr^{-1} $\simeq 40$ km s^{-1} at $r_0 = 1$ AU, we have $\eta_c \simeq 4(r/r_0)$ MV^{-1}. At $r > 0.05$ AU, $\eta_c \gtrsim 0.2$ MV^{-1}. On the other hand, because of resonance broadening, even 10 MV ions with $|\mu| \simeq 0$ can interact with waves at $\eta \lesssim 0.2$ MV^{-1}, albeit at reduced strength. For these reasons, we choose the P range as (10.4, 1878) MV for protons and (41.4, 1878) MV for He^{+2} ions, and for the Alfvén waves the η range $(4.87 \times 10^{-4}, 3.87 \times 10^{-1})$ MV^{-1}. Since the other minor ions are treated as test particles, their P ranges may be arbitrarily selected within the proton P range, e.g., (49.4, 1878) MV for O ions and (98.7, 1878) MV for Fe ions.

2.3.2. *Initial and Boundary Conditions on SEPs*

We start with empty SEP distributions

$$F_s(\mu, P, r, t = 0) \equiv 0 \tag{30}$$

and inject energetic ions at the traveling shock as described in § 2.2.2 (see eqs. [8] and [9]). At the fixed inner boundary $r = r_a$, the inward particle flux is matched by an outward flux from an isotropic distribution $F_{s,\rm out}$:

$$\int_{-1}^{\mu_*} d\mu(\mu v + V_{\rm sw}) F_s(\mu, P, r_a, t) = -\int_{\mu_*}^{1} d\mu(\mu v + V_{\rm sw}) F_{s,\rm out}(P, t) \ , \tag{31}$$

where μ_* is defined by

$$\mu_* v + V_{\rm sw} = 0 \ . \tag{32}$$

In other words, we solve equation (31) for $F_{s,\rm out}(P, t)$ and set the inner boundary condition:

$$F_s(\mu, P, r = r_a, t) = F_{s,\rm out}(P, t), (\mu > \mu_*) \ . \tag{33}$$

We consider an outer spatial boundary moving with the solar wind velocity $V_{\rm sw}$ and returning a prescribed fraction $\alpha_{\rm refl}$ ($\leq$1) of the outward flux through a "reflected" isotropic distribution $F_{s,\rm in}(P, t)$. The outer spatial boundary condition reads

$$F_s[\mu, P, r_b(t), t] = F_{s,\rm in}(P, t) \quad (\mu < \mu_*) \ , \tag{34}$$

where

$$r_b(t) = r_{b,0} + V_{\rm sw} t \tag{35}$$

gives the location of the boundary and $F_{s,\rm in}(P, t)$ is the solution to

$$\int_{-1}^{\mu_*} d\mu(\mu v + V_{\rm sw}) F_{s,\rm in}(P, t) = -\alpha_{\rm refl} \int_{\mu_*}^{1} d\mu(\mu v + V_{\rm sw}) F_s[\mu, P, r_b(t), t] \ . \tag{36}$$

We assume no energetic s-ions at and above the upper rigidity boundary at P_{Us}:

$$F_s(\mu, P = P_{Us}, r, t) = 0 \ . \tag{37}$$

There is no particle flux across $\mu = \pm 1$, and so

$$D_{\mu\mu} \frac{\partial F_s}{\partial \mu} = 0 \quad (\mu = \pm 1) \ . \tag{38}$$

Finally, for each ion species s, we advance F_s in time by solving the particle transport equation (20) with a time-dependent $D_{\mu\mu}$, subject to the initial condition given by equation (30) and the boundary conditions given by equations (33), (34), (37), and (38).

2.3.3. *Boundary and Initial Conditions on Alfvén Waves*

The wave evolution equation (17) for the modified spectral wave intensities $\Psi_\sigma(\eta, r, t)$ is to be solved subject to the following boundary and initial conditions. At the inner boundary at $r = r_a$, we assume a solar source of outward-propagating Alfvén waves having spectral magnetic intensities

$$I^\sigma(k, r_a, t) = I^{\sigma 0}(k) \equiv I_0^\sigma \left(\frac{k}{k_0}\right)^{-\delta} \tag{39}$$

over all wavenumbers k of interest and with k_0 a constant.

Hence, the boundary conditions at $r = r_a$ for Ψ_σ read

$$\Psi_\sigma(\eta, r_a, t) = \Psi_{\sigma 0}(\eta) \equiv 2I^{\sigma 0}[\eta B(r_a)] \frac{\eta V_{\sigma f}(r_a)}{\eta_0 V_{\rm A}(r_a)} , \quad (40)$$

where $\eta_0 = k_0/B_0$. The boundary condition at the low wavenumber boundary $\eta = \eta_L$ is

$$\Psi_\sigma(\eta_L, r) = \Psi_{\sigma L}(\eta_L) \equiv \Psi_\sigma(\eta_L, r, t = 0) , \quad (41)$$

where the right-hand side is fixed by the initial condition derived below.

The initial distributions of the outward Alfvén waves are specified as the steady state solutions of the wave evolution equation (23) with constant $\gamma_\sigma = \zeta_1 < 0$, without SEP-driven wave amplification. In the steady state boundary value problem below, we use for convenience the same symbols as in the time-dependent problem above, but we set the reference radius $r_0 = r_a$ instead of $r_0 = 1$ AU and use the shorthand $V_{\sigma f,0} = V_{\sigma f}(r_0)$ and $\eta_0 = k_0/B_0$. For analytical solution we restate the problem as

$$\frac{\partial}{\partial r}\left(V_{\sigma f}\Psi_\sigma\right) - \frac{d}{dr}\left[\ln\left(BV_{\sigma f}\right)\right]\eta\frac{\partial}{\partial \eta}\left(V_{\sigma f}\Psi_\sigma\right) = \frac{\zeta_1}{V_{\sigma f}}\left(V_{\sigma f}\Psi_\sigma\right) , \quad (42a)$$

subject to the boundary condition

$$\Psi_\sigma(\eta, r_0) = \Psi_{\sigma 0}(\eta) \equiv 2I^{\sigma 0}(\eta B_0)\frac{\eta V_{\sigma f,0}}{\eta_0 V_{\rm A,0}} . \quad (42b)$$

The solution to the boundary value problem given by equations (42a) and (42b) is

$$\Psi_\sigma(\eta, r) = \Psi_{\sigma 0}\left(\eta\frac{BV_{\sigma f}}{B_0 V_{\sigma f,0}}\right)\frac{V_{\sigma f,0}}{V_{\sigma f}}\exp\left(\int_{r_0}^{r} dr\frac{\zeta_1}{V_{\sigma f}}\right) , \quad (43a)$$

or, equivalently, in terms of the wave magnetic intensity

$$I^\sigma(k, r) = I_0^\sigma\left(\frac{kV_{\sigma f}}{k_0 V_{\sigma f,0}}\right)^{-\delta}\frac{BV_{\rm A}V_{\sigma f,0}}{B_0 V_{\rm A,0}V_{\sigma f}}\exp\left[\frac{\zeta_1(r - r_0)}{V_{\rm sw}}\right] \times \left(\frac{rV_{\rm sw} + r_0 V_{\rm A,0}}{r_0 V_{\rm sw} + r_0 V_{\rm A,0}}\right)^{-\zeta_1 r_0 V_{\rm A,0}/V_{\rm sw}^2} . \quad (43b)$$

The Alfvén speed $V_{\rm A}$ and the wave intensities I^σ are better estimated at $r_0 = 1$ AU than at $r_a = 0.05$ AU. Hence, we prescribe the initial conditions for I^σ via the steady state solution given by equation (43a) with the values of $V_{\rm A,0}$, $I^{\sigma 0}$, and B_0 at $r_0 = 1$ AU.

Finally, we advance the modified wave intensity Ψ_σ in time by solving the wave evolution equation (23) with a time-dependent γ_σ, subject to the initial condition given by equation (43a) and the boundary conditions given by equations (40) and (41).

3. NUMERICAL SCHEME

We solve numerically the coupled partial differential equations (20) and (23) in the initial boundary value problems formulated above using locally one-dimensional (LOD) finite-difference schemes. The modified particle phase-space densities F_s and the modified wave intensities Ψ_σ are approximated by their values on finite-difference grids constructed on the respective function domains. By replacing partial derivatives with finite differences, we approximate the partial differential equations with finite-difference schemes. The LOD method breaks the solution process down into a cycle of several steps, each step solving a simpler problem in one coordinate direction. Starting at the known time level t_n, we evaluate the diffusion coefficient $D_{\mu\mu}^n$ via numerical integration from the wave intensities Ψ_σ^n, and then we advance the particle density F_s^n of each ion species s to F_s^{n+1} at the next time level t_{n+1} after a cycle of computation. The advanced F_s^{n+1} of protons and He^{+2} are used to evaluate the wave growth rates γ_σ^{n+1} at t_{n+1} via numerical integration. Using γ_σ^{n+1}, each Ψ_σ^n at t_n is advanced to Ψ_σ^{n+1} at t_{n+1} after another cycle of computation. At this point, the process described above is repeated to advance all quantities from t_{n+1} to t_{n+2}.

The discretized energetic ion distributions $F_{s,i,j,l}^n \equiv F_s(\mu_i, P_\ell, r_j, t_n)$ are defined on the grid:

$$\mu_i = \left(i + \tfrac{1}{2}\right)\Delta\mu , \quad i = -I(1)I - 1 ; \quad (44)$$

$$\ln P_\ell = \ln P_1 + (\ell - 1)\Delta(\ln P) , \quad \ell = L_1(1)L_2 ; \quad (45)$$

$$r_j = r_a + (j - 1)\Delta r , \quad j = 1(1)J . \quad (46)$$

We usually choose $I = 20$ and $\Delta\mu = I^{-1}$ for the μ grid; $r_a = 0.05$ AU and $\Delta r = 0.0125$ AU for the r grid; and for the logarithmic P grid, $P_1 = 10.375$ MV, $\Delta(\ln P) = (\ln 2)/8$ with P in MV, $L_1 = 1$ and $L_2 = 61$ for protons, and $L_1 = 9$ and $L_2 = 61$ for He^{+2}. For other ion species, which are treated as test particles, we may employ only a subset (e.g., every other grid point) of the P grid to save storage and CPU time. At the "basic" times t_n ($n = 0, 1, \ldots$), the diffusion coefficients $D_{\mu\mu}^n$ are computed from the wave intensities, and the wave growth rates γ_σ^n are computed from the particle densities. The time levels t_n are not spaced evenly apart because the time steps used to advance the SEP and Alfvén wave distributions are set dynamically.

The discretized wave distributions $\Psi_{\sigma,m,j}^n \equiv \Psi_\sigma(\eta_m, r_j, t_n)$ are approximated on the (η_m, r_j, t_n) grid, where r_j and t_n are as described above, and the η grid is logarithmically spaced:

$$\log_{10}\eta_m = \log_{10}\eta_1 + (m - 1)\Delta(\log_{10}\eta) , \quad m = 1(1)M_j . \quad (47)$$

We mostly employ $\Delta(\log_{10}\eta) = 0.05$ with η in units of $\rm MV^{-1}$ and $\eta_1 = 4.87 \times 10^{-4}$ $\rm MV^{-1}$. As discussed in § 2.3.1, at small r the upper η boundary may be limited by an r-dependent upper cutoff due to wave steepening at high wavenumbers. Hence, the upper limit M_j to the wavenumber index m depends on the r index j, subject to a maximum of $M_j = 58$, corresponding to $\eta_{M_j} = 3.868 \times 10^{-1}$ $\rm MV^{-1}$.

The particle transport equation (20) is of the form

$$\frac{\partial F}{\partial t} - (D_P + D_\mu + D_r)F = G , \quad (48)$$

where D_r, D_μ, and D_P are partial differential operators involving the r, μ, and P derivatives, respectively.

We use the three-step LOD scheme

$$F^{n+1/3} = (I + A_r)(I + \tau\Lambda_r)(F^n + \tau G^n), \quad (49a)$$

$$F^{n+2/3} = (I + A_\mu)\left(I - \theta\tau\Lambda_{\mu d}\right)^{-1} \times \left[I + \tau\Lambda_{\mu f} + (1 - \theta)\tau\Lambda_{\mu d}\right]F^{n+1/3}, \quad (49b)$$

$$F^{n+1} = (I + A_P)(I + \tau\Lambda_P)F^{n+2/3}, \quad (49c)$$

where $F^n = F(t_n)$, $F^{n+1} = F(t_n + \tau)$, $G^n = G(t_n)$, $F^{n+1/3}$

and $F^{n+2/3}$ are iterates, and the difference operators are defined by

$$\Lambda_r F_{i,j,\ell} = \frac{(\mu_i v_\ell + V_{\rm sw})(F_{i,j-1,\ell} - F_{i,j,\ell})}{\Delta r} , \quad (50a)$$

$$\Lambda_P F_{i,j,\ell} = \frac{(1-\mu_i^2) V_{sw} (F_{i,j,\ell+1} - F_{i,j,\ell})}{(r_j \Delta \ln P)} , \quad (50b)$$

$$\Lambda_{\mu f} F_{i,j,\ell} = [(1-\mu_{i-1/2}^2) F_{i-1,j,\ell} - (1-\mu_{i+1/2}^2) F_{i,j,\ell}] \frac{v_\ell}{(r_j \Delta\mu)} , \quad (50c)$$

$$\Lambda_{\mu d} F_{i,j,\ell} = \frac{1}{(\Delta\mu)^2} [D_{i+1/2,j,\ell}(F_{i+1,j,\ell} - F_{i,j,\ell}) - D_{i-1/2,j,\ell}(F_{i,j,\ell} - F_{i-1,j,\ell})] . \quad (50d)$$

The above scheme is first order in time. In equations (50a)–(50d), we have omitted the time index in all F and the subscript $\mu\mu$ in $D_{i\pm1/2,j,\ell}$. In the explicit scheme given by equation (49a), Λ_r is the first-order upwind divided difference operator and A_r a nonlinear flux-limited antidiffusion operator (Boris & Book 1976). Analogous descriptions apply to Λ_P and A_p in the explicit scheme given by equation (49c). In the implicit scheme given by equation (49b), $\Lambda_{\mu f}$ is the upwind divided difference operator for magnetic focusing, $\Lambda_{\mu d}$ is the central divided difference operator for μ diffusion, A_μ is a flux-limited antidiffusion operator, θ and $1-\theta$ are the weights assigned to $\Lambda_{\mu d} F^{n+2/3}$ and $\Lambda_{\mu d} F^{n+1/3}$, respectively, and $0 < \theta \lesssim 1$. We generally set $\theta = 1$. All three schemes are positive and conservative.

Using discretized boundary and initial conditions, it is straightforward to solve the explicit equations in the schemes given by equations (49a) and (49c), followed by antidiffusive flux correction to reduce numerical dispersion errors. For the implicit system given by equation (49b) we first solve the tridiagonal system of equations in

$$(I - \theta\tau\Lambda_{\mu d}) F^* = \{I + [\tau\Lambda_{\mu f} + (1-\theta)\tau\Lambda_{\mu d}]\} F^{n+1/3} \quad (51)$$

for F^*, and then we apply antidiffusive flux correction: $F^{n+2/3} = (I + A_\mu) F^*$.

In principle, the solution for the time-splitting scheme above is as follows. For each value of ℓ, equation (49a) is solved for $F_{i,j,\ell}^{n+1/3}$ sweeping in the j-direction for each value of i. Then equation (49b) is solved for $F_{i,j,\ell}^{n+2/3}$, sweeping in the i-direction for each value of j. Finally for all pairs (i, j), equation (49c) is solved for $F_{i,j,\ell}^{n+1}$, completing the three-step cycle. The actual procedure followed is modified from the above by using different values of τ in accordance with the different timescales for the different processes and in different parts of the domain.

The SEPs and Alfvén waves are coupled after $\Delta t_n = t_{n+1} - t_n$, which is set dynamically. Besides satisfying numerical stability requirements, Δt_n is set small enough that Ψ_σ does not grow too much before its effects (through $D_{\mu\mu}$) are fed back to the SEPs, and $|dF_s/d\mu|$ does not become too large before its effects (through γ_σ) are fed back to the waves.

We consider next the numerical solution of the wave evolution equation (23). Again, we use operator splitting to obtain the following LOD scheme for wave evolution:

$$\Psi^{n+1/3} = \left(1 - \frac{\tau\gamma}{2}\right)^{-1} \left(1 + \frac{\tau\gamma}{2}\right) \Psi^n , \quad (52a)$$

$$\Psi^{n+2/3} = (I + A_\eta)(I + \tau\Upsilon_\eta) \Psi^{n+1/3} , \quad (52b)$$

$$\Psi^{n+1} = (I + A_r)(I + \tau\Upsilon_r) \Psi^{n+2/3} , \quad (52c)$$

where Υ_η and Υ_r are forward difference operators defined as follows:

$$\Upsilon_\eta \Psi_{m,j} = (2V_{\rm sw} + 3V_{{\rm A},j}) \frac{(\Psi_{m-1,j} - \Psi_{m,j})}{[r_j (\ln 10) \Delta(\log_{10}\eta)]} , \quad (53a)$$

$$\Upsilon_r \Psi_{m,j} = \frac{[(V_{\rm sw} + V_{{\rm A},j-1/2}) \Psi_{m,j-1} - (V_{\rm sw} + V_{{\rm A},j+1/2}) \Psi_{m,j}]}{\Delta r} . \quad (53b)$$

We now have to specify the value of τ. Recall that we have set Δt_n as the time step to couple wave excitation and SEP streaming, and so it appears appropriate to set $\tau = \Delta t_n$ in equation (52a). However, Δt_n is much smaller than the timescales of wave transport in equations (52b) and (52c). Hence, we modify the scheme given by equations (52a)–(52c) as follows. For every basic time step Δt_n, we implement wave amplification

$$\Psi^{n+1} = \left(1 - \frac{\Delta t_n \gamma}{2}\right)^{-1} \left(1 + \frac{\Delta t_n \gamma}{2}\right) \Psi^n \quad (54)$$

and, less frequently, the following two-step cycle for the η and r transport of waves:

$$\Psi^{k+1/2} = (I + A_\eta)(I + \Delta t_{\eta r} \Upsilon_\eta) \Psi^k , \quad (55a)$$

$$\Psi^{k+1} = (I + A_r)(I + \Delta t_{\eta r} \Upsilon_r) \Psi^{k+1/2} , \quad (55b)$$

stepping from one basic time level t_k to a later basic time level t_{k+1} using the larger time step $\Delta t_{\eta r}$. The latter time step is chosen to satisfy the stability condition

$$\Delta t_{\eta r} \lesssim \min_j \left\{ \frac{\Delta r}{(V_{\rm sw} + V_{{\rm A},j+1/2})}, \frac{r_j (\ln 10) \Delta(\log_{10}\eta)}{(2V_{\rm sw} + 3V_{{\rm A},j})} \right\} . \quad (56)$$

The SEPs and Alfvén waves are coupled via the wave-particle resonance function $R_{\mu\mu}^\sigma$ (Appendix A) in equations (26) and (27). We evaluate the single and double integrals in the expressions for $D_{\mu\mu}$ and γ_σ numerically using the extended trapezoidal rule. To save storage and CPU time, we integrate only over regions where the function $R_{\mu\mu}^\sigma \Omega/\gamma$ lies above a preset fraction (0.01–0.02) of its maximum value.

4. RESULTS

We present in some detail the calculated results and interpretations for one set of model parameters (case 1) to provide a comprehensive overview of the model simulation, followed by some contrasting results from case 2 in which a few parameters are changed. Our purpose is to describe a new mode of SEP transport through self-amplified waves with relevance to the observation of SEP abundance variation. Parameter studies and application of the model to SEP events will be reported elsewhere. Table 1 lists the model parameters and their values in cases 1 and 2. The values of $n_{\rm H,0}$ and $V_{\rm A,0}$ there imply $B_0 = 3.41$ nT at $r = 1$ AU. The results presented in this paper apply to one magnetic flux tube. A spacecraft samples in time a progression of "corotating" flux tubes with different connections to the evolving shock front. The reader should keep this in mind when comparing the results here with specific observation.

TABLE 1
MODEL PARAMETERS

PARAMETERS	VALUES	
	Case 1	Case 2
Solar wind velocity, V_{sw} (km s^{-1})	333	333
Shock velocity, V_{sh} (km s^{-1})	1667	1667
Initial shock location, $r_{sh,0}$ ($R_\odot$)	13.4	13.4
Inner boundary location, r_a ($R_\odot$)	10.7	10.7
Initial outer moving boundary location,[a] r_b (AU)	2.0	2.0
Outer boundary reflection coefficient, α_{refl}	0.95	0.95
Plasma proton number density at 1 AU,[b,c] $n_{H,0}$ (cm^{-3})	5	5
O charge state,[d] Q_O	6.67	6.67
Fe charge state,[d] Q_{Fe}	13.88	13.88
Seed particle fraction,[e] b	5×10^{-3}	2.5×10^{-3}
Ion seed energy per amu,[e] E_0/A (keV amu^{-1})	5	5
Initial SEP source spectral index,[e] α_0	4	4
Radial rate of change of α,[e] α' (AU^{-1})	2.5	0.5
Initial e-folding energy of proton source,[f] $E_{e,0}$ (MeV)	60	2000
Alfvén speed at 1 AU,[c,g] $V_{A,0}$ (km s^{-1})	33.3	33.3
Ambient wave intensity at η_0 and 1 AU,[h] I_0^σ (MeV cm^{-2})	2.5×10^3	2.5×10^3
Reference modified wavenumber, η_0 (MV^{-1})	0.02308	0.02308
Ambient wave spectral index, δ	1.667	1.667
Rate of change of ambient Alfvén waves, ζ_1 (hr^{-1})	−0.01	−0.01
Resonance broadening parameter, a	0.10	0.10

[a] Moving with solar wind velocity V_{sw}.
[b] For minor ions, $n_{s,0}$ is obtained from $n_{H,0}$ using known coronal abundances (Reames 1999). Note $n_s \propto r^{-2}$.
[c] $B_0 = V_{A,0}(4\pi m_p n_{H,0})^{1/2}$ is determined by $V_{A,0}$ and $n_{H,0}$.
[d] See text for reason of fractional charge state.
[e] Identical for all species.
[f] $E_e \propto [r_{sh}(t)]^{-1}$. For s-ions, $E_e^s/A_s = Q_s E_e/A_s$.
[g] $V_A(r) \propto r^{-1}$.
[h] Same for $\sigma = R+$ and $L+$.

We begin with case 1, in which the accelerated SEP source spectra initially steepen beyond $\sim Q_s/A_s$ times 60 MeV, and the power-law spectral index α softens at the rate of 2.5 AU^{-1} as the shock advances. At $t = 0$ the continuous injection of multispecies SEPs is initiated over a broad energy range at the traveling shock. These SEPs propagate through the IP medium, interacting with Alfvén waves as they go. Figures 1–7 provide an overview of the coupled evolution of SEPs and Alfvén waves. Figure 1 shows the time histories of SEP differential intensities $j_{E/A}$ and abundance ratios at $r = 1.15$ AU for seven energies per amu. The bottom panels of Figure 2 illustrate the dispersal of the SEPs through successive snapshots of the radial distributions of SEPs. The evolution of the Alfvén waves is illustrated in Figures 3 (*top panels*), 4, and 5. These plots show the wave spectra at successive epochs at fixed locations relative to the Sun and relative to the traveling shock. The coupling of the SEPs and Alfvén waves may be studied by comparing the successive rigidity profiles of the particle mean free path λ (Fig. 3, *bottom panels*) with the corresponding wave spectra (Fig. 3, *top panels*) and by comparing the successive λ-r profiles (Fig. 2, *top panels*) with the corresponding $j_{E/A}$-r profiles (Fig. 2, *bottom panels*). Figure 6 describes the evolution of the energy spectra of SEP intensities and abundance ratios. Figure 7 compares the time variations of the anisotropies of SEP ions at four energies per amu at $r = 1.15$ AU. These features will be described and interpreted in terms of dynamic wave-particle interaction below.

4.1. *Time and Radial Variation of SEP Intensities*

The left-hand and middle panels of Figure 1 show the time histories of the differential intensities j^H, j^{He}, j^O, and j^{Fe} of H^+, He^{+2}, $O^{+6.67}$, and $Fe^{+13.9}$ ions, respectively, at $r = 1.15$ AU at 0.32, 0.65, 1.30, 2.59, 5.18, 10.3, and 20.5 MeV amu^{-1}. For all ion species, with increasing energy, the differential intensity rises earlier and faster, peaks earlier at lower maximum, and decays more rapidly. This is due to the following: velocity dispersion, pitch-angle scattering rate decreasing with energy in the initial Kolmogorov wave spectra, amplified waves having weaker influence on higher rigidity particles, and descending source particle intensity energy spectra. Note that all calculated $j_{E/A}$ are given in (cm^2 s sr MeV amu^{-1})$^{-1}$, not arbitrary units. In this model, we specify the source spectra of H^+, He^{+2}, $O^{+6.67}$, and $Fe^{+13.9}$ ions as functions of v, P, and t (eq. [8]). The elemental composition of the source is normalized to the coronal abundances given by Reames (1999) at the seed energy $E_0/A = 5$ keV amu^{-1} and varies with energy per amu as a result of the A/Q-dependent exponential factor (eq. [8]). The proton source strength affects all calculated particle intensities through proton-amplified IP Alfvén waves. Except at the highest rigidities, the intensity rise in Figure 1 is much slower than that without proton-driven amplification, and except at the lowest energies, the intensity decay is largely determined by the moving outer boundary, placed initially at $r = 2$ AU.

A view of the propagation of the SEPs through the IP medium is provided in the bottom panels of Figure 2,

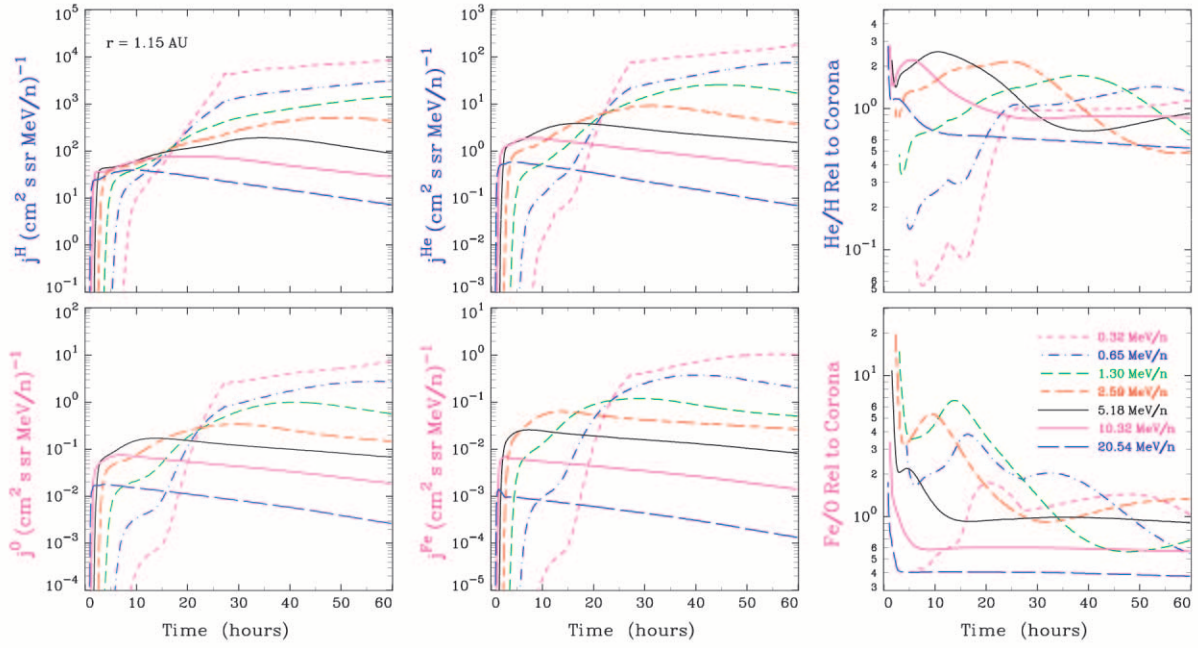

FIG. 1.—*Top panels, left to right:* Time histories of proton and He^{+2} differential intensities, and He/H ratio normalized to coronal values at $r = 1.15$ AU. *Bottom panels, left to right:* As above for $O^{+6.7}$ and $Fe^{+13.9}$, and normalized Fe/O ratio.

showing successive snapshots of the radial profiles of the proton, $O^{+6.67}$, and $Fe^{+13.9}$ intensities at 2.6 MeV amu^{-1}. These snapshots of the radial profiles of the particle intensity j are matched by concurrent snapshots of the radial profiles of the particle mean free path λ in the top panels of Figure 2. Comparison of the j-r and λ-r profiles shows that the regions of greatly reduced λ retard outward SEP propagation, forming behind them "reservoirs" of quasi-trapped particles with almost flat spatial intensity profiles, whereas in and beyond these regions the intensities fall steeply with r. With the passage of time, the depressions in λ move outward, becoming shallower and less effective in retarding

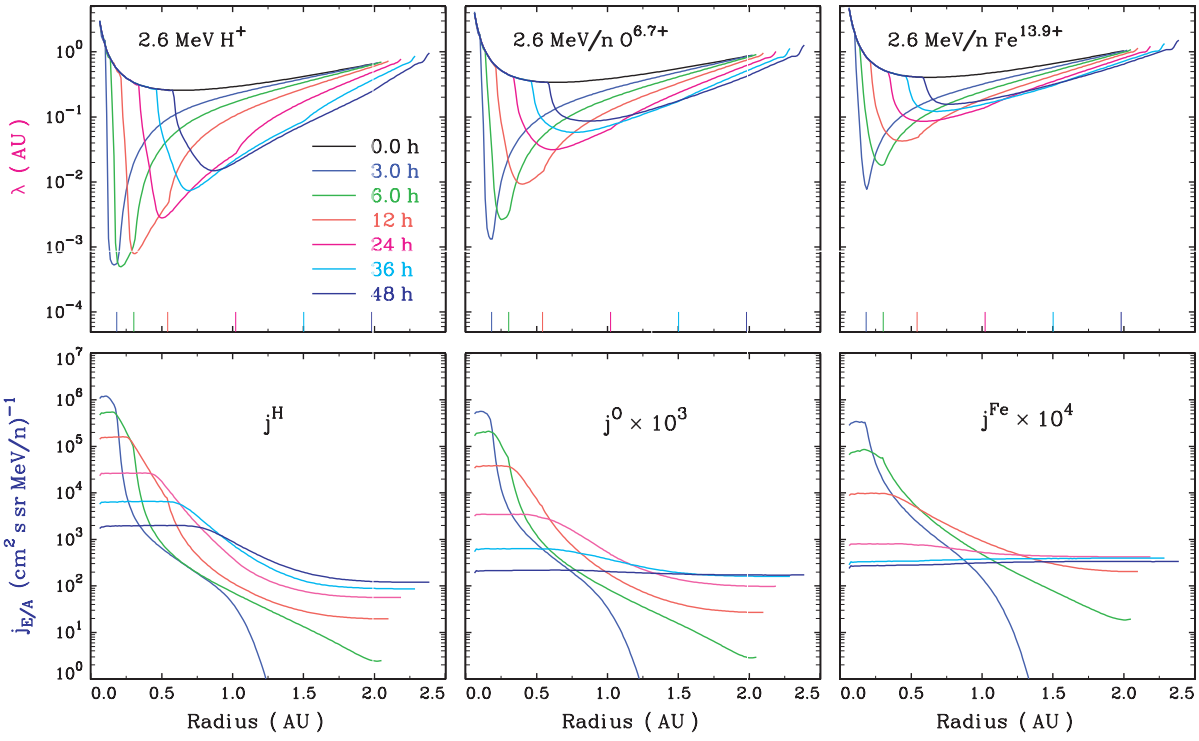

FIG. 2.—Radial profiles of the mean free paths λ (*top panels*) and differential intensities $j_{E/A}$ (*bottom panels*) of 2.6 MeV amu^{-1} H^+, $O^{+6.7}$, and $Fe^{+13.9}$ ions (*left, middle, and right*) at indicated times. Shock locations are indicated by short vertical lines in the top panels. The regions of small λ slow outward SEP transport, imposing steep spatial intensity gradients in and beyond these regions. The intensity profiles are almost flat in the weak scattering regions behind.

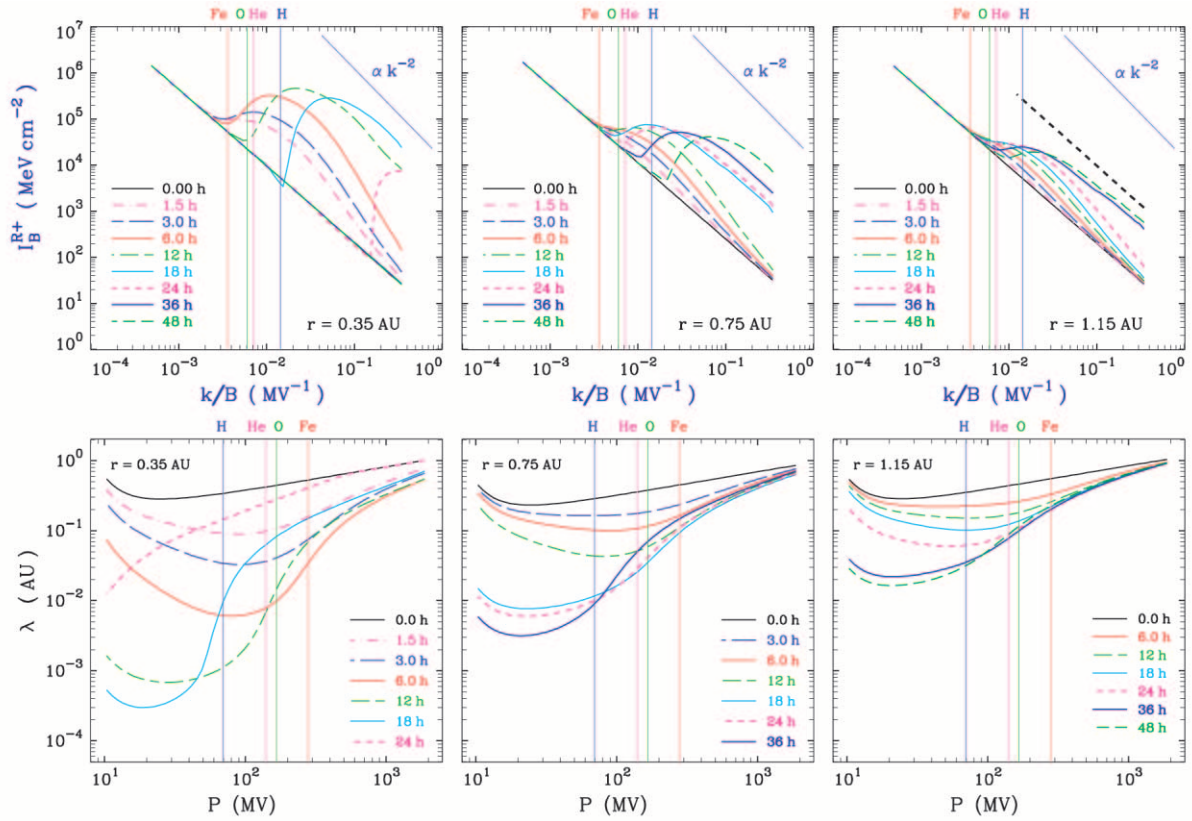

FIG. 3.—*Top panels:* Evolving I^{R+} spectra at $r = 0.35$, 0.75, and 1.15 AU. The vertical lines give from left to right, respectively, the resonant wavenumbers for 2.6 MeV amu^{-1} $Fe^{+13.9}$, $O^{+6.7}$, He^{+2}, and H^{+} ions at $\mu = 1$. The resonant wavenumber ranges are located near $k/B \approx (|\mu|P)^{-1}$, moving to the left with increasing energy, and to the right and broadening as $|\mu|$ decreases. The thick black dashed line in the third panel shows a typical magnetic power spectrum observed on the *Wind* spacecraft at 1 AU for 1995 January 30, 1300–1400 UT (Leamon et al. 1998). *Bottom panels:* Evolving λ-P profiles, calculated from I^{R+} above and I^{L+} (not shown). The vertical lines give (from left to right) the rigidities of H^{+}, He^{+2}, $O^{+6.7}$, and $Fe^{+13.9}$ ions at 2.6 MeV amu^{-1}.

outward SEP propagation. The particle intensity levels fall monotonically in the expanding reservoirs, while outside the reservoirs the intensities and their radial gradients first rise and then fall. The dramatic dips in λ from the initial λ-r profiles are due to wave amplification by streaming energetic protons, while the rise and outward motion of these dips are due to wave transport. These issues will be discussed later in connection with the evolution of the Alfvén wave distributions and the evolution of λ-P profiles.

4.2. *Time Variation of SEP Abundance Ratios*

The He/H and Fe/O ratios are calculated from j^{H}, j^{He}, j^{O}, and j^{Fe} at $r = 1.15$ AU and displayed in the right-hand panels of Figure 1. In contrast to the relatively simple behavior of the SEP intensities, the abundance ratios show complex temporal and energy dependences, and Fe/O ratios differ significantly from He/H. Before we discuss the results on abundance ratios, a few prior comments are in order. First,

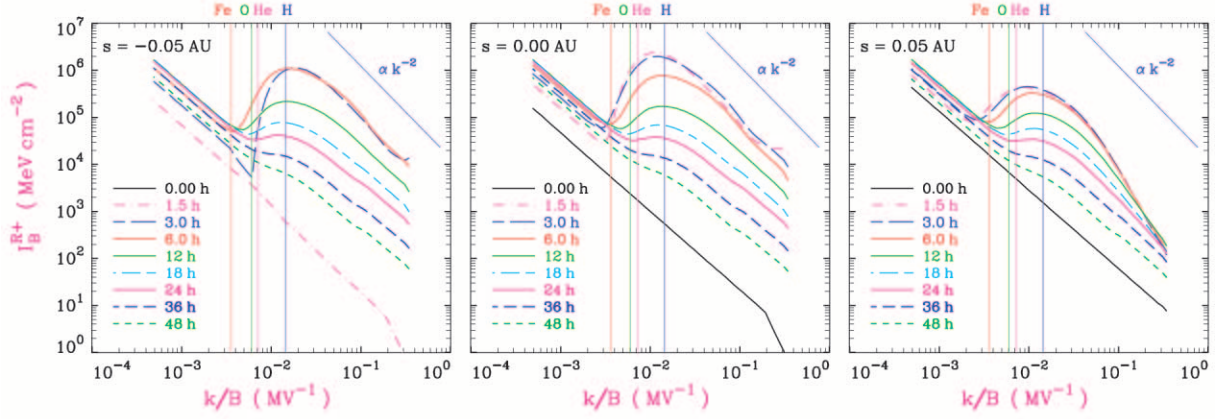

FIG. 4.—Time evolution of I^{R+} at $s = -0.05$, 0, and 0.05 AU upstream from the traveling shock. The vertical lines give from left to right the resonant wavenumbers for 2.6 MeV amu^{-1} $Fe^{+13.9}$, $O^{+6.7}$, He^{+2}, and H^{+} ions at $\mu = 1$. The resonant wavenumber ranges are located near $k/B \approx (|\mu|P)^{-1}$, moving to the left with increasing energy, and to the right and broadening as $|\mu|$ decreases.

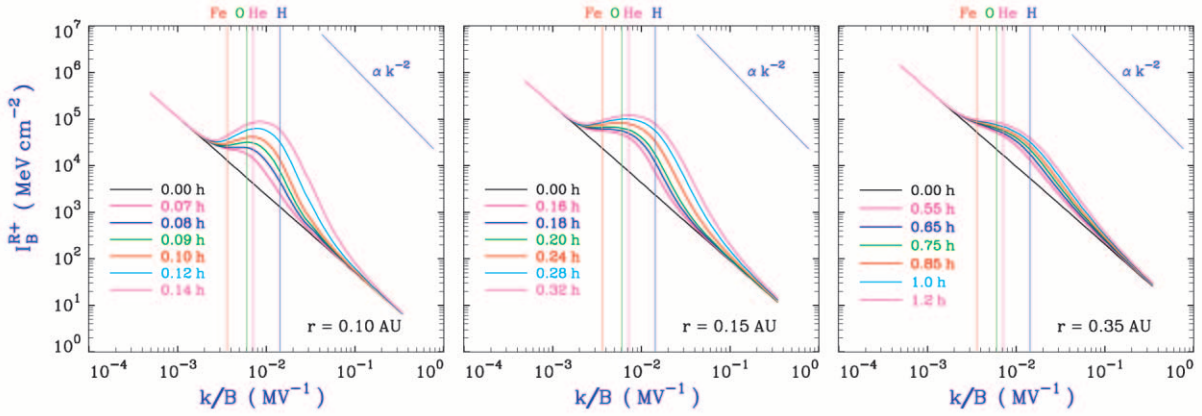

FIG. 5.—Evolution of I^{R+} vs. k/B at $r = 0.10$, 0.15, and 0.35 AU upstream from the traveling shock. The vertical lines give from left to right, respectively, the resonant wavenumbers for $Fe^{+13.9}$, $O^{+6.7}$, He^{+2}, and H^{+} ions at 2.6 MeV amu^{-1} and $\mu = 1$.

in this paper, all calculated He/H and Fe/O ratios are normalized to the coronal values of 0.036 and 0.134, respectively (Reames 1999). Note, however, that the low time asymptotic values of the calculated He/H and Fe/O ratios at high energies in case 1 are due partly to the A/Q-dependent e-folding energies in the source ratio (eq. [8]). Second, we have specified the nonphysical fractional charge states of 13.88 and 6.667 for O and Fe ions so that their rigidities fall on the ln P grid at the energies per amu shown in Figure 1 to avoid errors in interpolating for abundance ratios due to velocity dispersion. The assumed ionic charge states are typical mean values in large gradual SEP events (e.g., Luhn et al. 1984; Leske et al. 1995) and thus appropriate for qualitative illustration of the kinds of effects that can arise. However, both higher and lower mean Fe charge states have been reported (Larson et al. 1999; Möbius et al. 2002; Tylka et al. 2000), and a lower Fe charge state will cause even larger variations in the Fe/O than shown here. The broad distribution of Fe charge states may also have to be taken into account before comparing with data (Tylka et al. 2001). Finally, in this paper, the atomic mass units are normalized to $A = 1$ for protons; thus, the A/Q values of protons, He^{+2}, $O^{+6.667}$, and $Fe^{+13.88}$ are 1, 1.986, 2.378, and 3.999, respectively.

Since the abundance ratio is calculated at equal energy per amu (equivalently, equal velocity), it is a sensitive

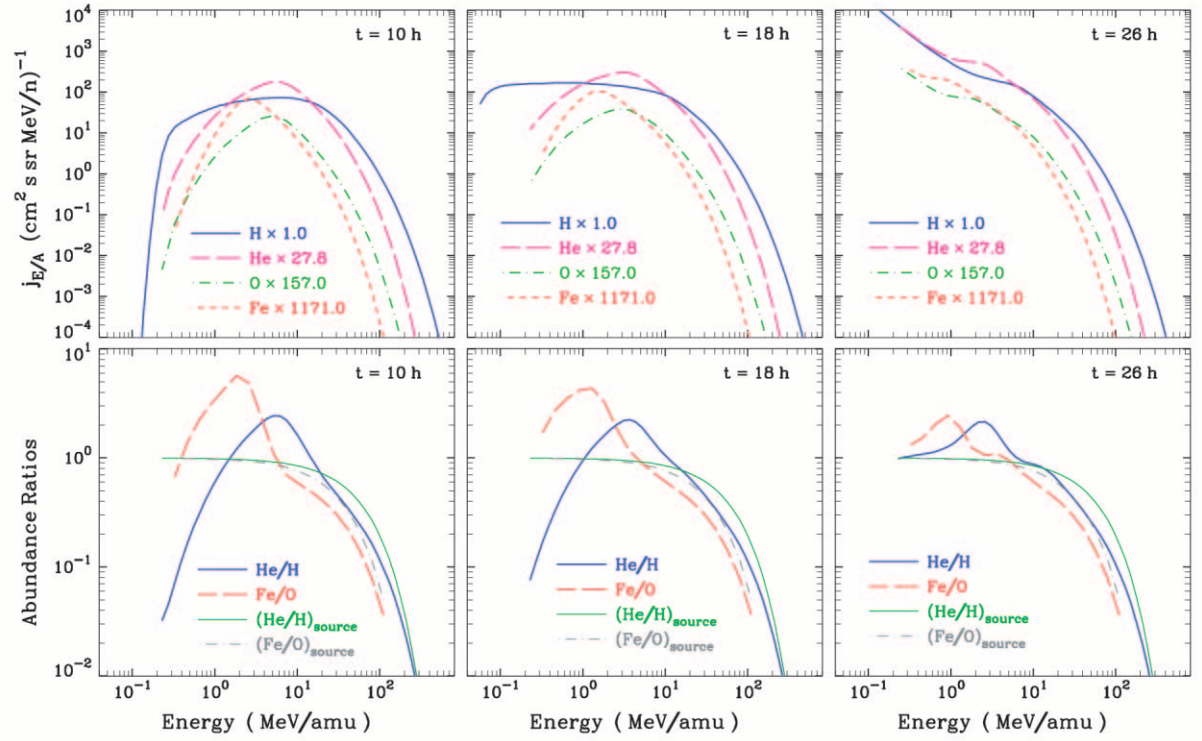

FIG. 6.—*Top panels:* differential intensity spectra of protons, He^{+2}, $O^{+6.7}$, and $Fe^{+13.9}$ ions at $t = 10$, 18, and 26 hr, at $r = 1.15$ AU. *Bottom panels:* Corresponding spectra of He/H and Fe/O ratios. The He/H and Fe/O source spectra at $t = 0$ are shown for comparison. All ratios are normalized to coronal values.

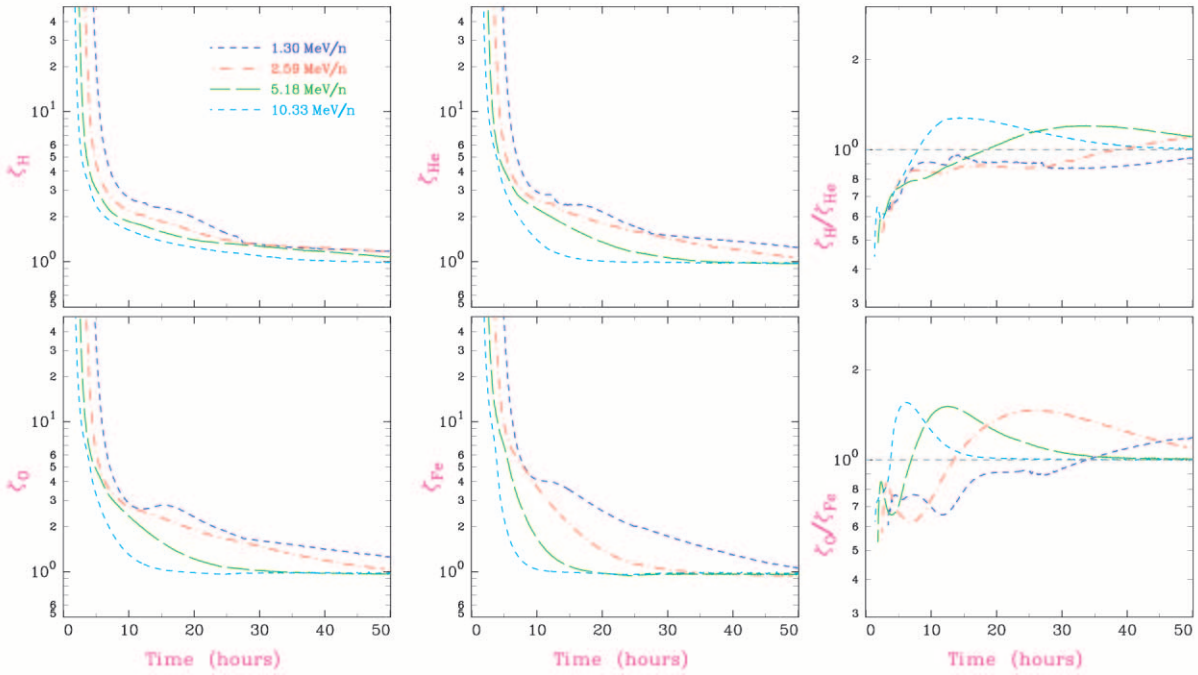

FIG. 7.—*Top panels, left to right:* time histories of the front-to-back ratios ζ_H, ζ_{He} of H^+ and He^{+2} ions, respectively, and ζ_H/ζ_{He}, at $r = 1.15$ AU and indicated energies. *Bottom panels, left to right:* As in the top panels, but for $O^{+6.7}$ and $Fe^{+13.9}$ ions.

measure of the difference in the pitch-angle scattering experienced by the two ion species due entirely to the difference in their rigidities. The rigidity ratio equals the ratio of the A/Q values. In the absence of SEP-driven amplification of the Kolmogorov wave spectra, the abundance ratio of high- to low-rigidity (high- to low-A/Q) ions, normalized to the source ratios, falls monotonically in time from $\gg 1$ and asymptotes toward a value less than unity. This can be demonstrated analytically for the spatial diffusion model (Appendix C). By contrast, the complex time variation of the He/H and Fe/O ratios in Figure 1 is due to particle transport through time-dependent proton-amplified waves. We interpret below the time variation of He/H and Fe/O in terms of the evolving mean free path λ as a function of rigidity P. A detailed discussion in terms of resonant wave-particle interaction is given after the presentation of the Alfvén wave distributions.

4.3. *Evolution of λ-P Profiles*

The evolving λ-P profiles at $r = 0.35$, 0.75, and 1.15 AU are shown in the bottom panels of Figure 3. As a result of proton-driven wave growth, λ falls in time, deeper at smaller r where wave growth is larger, and nonuniformly as a function of P because of the velocity dispersion of the exciting energetic protons and the P dependence of the proton source. The initially positive gradient $\partial\lambda/\partial P$ not only grows at some rigidities but also decreases to less than 0 at low rigidities, in a strongly r- and t-dependent fashion. At 10.3 and 20.5 MeV amu^{-1}, $O^{+6.7}$ and $Fe^{+13.9}$ ions have rigidities greater than 330 MV, where λ_O, the mean free path of $O^{+6.7}$, is shorter than λ_{Fe}, that of $Fe^{+13.9}$, and the ratio λ_{Fe}/λ_O does not vary greatly with time. Consequently, Fe/O at $r = 1.15$ AU decays monotonically from greater than 1 to less than 1 (Fig. 1, *bottom right panel*), similar to the behavior for transport in time-independent Kolmogorov wave spectra (Appendix C). Note that at these energies the Fe/O source ratio is already somewhat lower than unity.

From 650 keV amu^{-1} to 2.6 MeV amu^{-1}, however, $O^{+6.7}$ and $Fe^{+13.9}$ ions span 83–279 MV, where λ falls steeply with time while $\partial\lambda/\partial P > 0$ increases. For example, at $r = 0.35$ AU, λ_{Fe}/λ_O at 2.6 MeV amu^{-1} increases from 1.19 at $t = 0$ to a maximum of $\approx$6 at $t \approx 12$ hr (Fig. 3, *bottom left panel*). For time-independent $\lambda_{Fe}/\lambda_O > 1$, as the early faster rise of j^{Fe} gives way permanently to a slower rise or faster decay relative to j^O, Fe/O falls continuously to less than 1. Here, in contrast, as λ_O falls rapidly while λ_{Fe}/λ_O rises, the rise of j^O becomes slower than that of j^{Fe} and Fe/O rebounds to an energy-dependent peak (Fig. 1).

At the even lower energy of 320 keV amu^{-1}, Fe/O starts from less than 1 and increases with time. This behavior, which is different from that calculated at higher energies, is easily understood in terms of the λ-P plot (Fig. 3, *bottom panels*): except for the few earliest $Fe^{+13.9}$ ions that escape (whose intensity is too small to detect), these slow $Fe^{+13.9}$ ions encounter shorter λ than $O^{+6.7}$ ions in the 59–99 MV resonant rigidity range where $\partial\lambda/\partial P < 0$ (Fig. 3, *bottom left panel*). The time variation of the He/H ratio at various energies may be interpreted similarly, noting that at the same velocity, protons and He^{+2} have lower rigidities than $O^{+6.7}$ and $Fe^{+13.9}$. The rigidities of H^+, He^{+2}, $O^{+6.7}$, and $Fe^{+13.9}$ ions at 2.59 MeV amu^{-1} are marked by vertical lines in the λ-P plots in Figure 3. These lines move to the right or left at higher or lower energies per amu with their separations remaining fixed.

Using different model parameters, we fit reasonably well the concurrent time histories of j^H, j^{He}, j^O, j^{Fe}, Fe/O, and He/H, observed on the *Wind* spacecraft in the contrasting 1998 September 30 and 2000 April 4 gradual events (Ng et al. 2001). Earlier, attempts were made with a prototype model, which neglected solar wind convection and wave transport, to reproduce the complex time variations of the

abundance ratios of various minor ion species relative to oxygen as well as He/H observed on *Wind* in the 1998 April 20 gradual event (Ng et al. 1999a; Tylka 2001). The results are in good semiquantitative agreement with the observation, in particular, the complex A/Q-dependent rebounds and the contrasting He/H and Fe/O histories.

The above account paints with a broad stroke the influence of the amplified waves on SEP transport, as manifested in the SEP intensities and abundance ratios, via the evolution of λ-r profiles (Fig. 2, *top panels*) and λ-P profiles (Fig. 3, *bottom panels*). Note, however, that the concept of mean free path is not always applicable, especially in the early phase, when the SEPs arriving at distant locations have been confined to $\mu > 0$. The evolution of λ is of course due to the amplification of IP Alfvén waves, to which we next focus our attention.

4.4. *Alfvén Wave Spectra*

As the SEPs travel out from the inner heliosphere, they interact with and amplify IP Alfvén waves (eq. [19]). The resulting wave evolution is illustrated in Figures 3 and 4. The top panels of Figure 3 display, at nine successive epochs, the magnetic intensity spectrum of the outward right-hand polarized Alfvén waves (I^{R+} vs. k/B) at $r = 0.35$, 0.75, and 1.15 AU. Figure 4 shows at the same epochs the I^{R+} spectrum at moving locations $s = -0.05$, 0, and 0.05 AU upstream of the traveling shock. We may examine the close coupling of the SEP distributions (Figs. 1 and 2) and the Alfvén wave distributions (top panels of Fig. 3 and Fig. 4) through the quasilinear wave-particle resonance condition $k/B \approx (\mu P)^{-1}$. For example, the proton source spectrum (eq. [8], with $\alpha_0 = 4$ and $E_{e,0} = 60$ MeV) contains few particles at $\gtrsim$500 MV; consequently, there is insignificant wave excitation at $k/B < 2 \times 10^{-3}$ MV^{-1} in all wave spectra.

Wave growth is very strong in the inner heliosphere but diminishes quickly with r. The top right panel of Figure 3 shows that the amplified I^{R+} spectrum at $r = 1.15$ AU stays below the "typical" magnetic field power spectrum evaluated by Leamon et al. (1998) from observation aboard the *Wind* spacecraft at 1 AU for the period 1995 January 30, 1300–1400 UT.[4] We have translated the observed power spectrum to our plot using the following relations:

$$\frac{k}{B} = \frac{2\pi\nu}{B(V_{\rm sw}\cos\theta_{BV} + V_{\rm A})}\ , \tag{57}$$

$$I_k = \frac{I_\nu(V_{\rm sw}\cos\theta_{BV} + V_{\rm A})}{2\pi}\ , \tag{58}$$

where ν is the wave frequency in the spacecraft frame, θ_{BV} is the angle between the solar wind velocity and the mean magnetic field, and I_k and I_ν are the spectral density with respect to wavenumber and frequency, respectively.

At the traveling shock, the I^{R+} spectrum (Fig. 4, *middle panel*) is amplified at $k/B \gtrsim 1 \times 10^{-2}$ MV^{-1} by 3 orders of magnitude within a fraction of an hour to a modified spectrum that is slightly steeper than k^{-2} at $k/B > 4 \times 10^{-2}$ MV^{-1} but that rolls down to join the unamplified Kolmogorov spectrum on the left at $k/B \lesssim 2 \times 10^{-3}$ MV^{-1}. At larger distances upstream of the shock, the waves have less time to grow, the Alfvén speed and SEP streaming are smaller, and the SEP spectra harden. All these factors lead to slower wave growth, especially at high k/B (see eq. [19]); consequently, at $s = 0.05$ AU, the early amplified wave spectrum is lower and steeper (Fig. 4, *right-hand panel*).

As we follow the shock outward, previously greatly amplified waves at the shock are swept downstream (Fig. 4, *left-hand panel*) and replaced by less strongly amplified upstream waves (Fig. 4, *right-hand panel*), which has since been further amplified, especially at the higher wavenumbers. As the SEP source spectra soften and decay (eq. [8]) and the Alfvén speed near the shock decreases, the SEP-driven wave growth rate (eq. [19]) falls and the wave spectrum at the shock flattens and decays.

The careful reader may have noticed in Figure 4 that, at fixed s from the traveling shock, the unamplified wave intensity at $k/B \lesssim 2 \times 10^{-3}$ MV^{-1} rises gradually in time. These unamplified waves are from the ambient distribution, specified via the steady state WKB solution (eq. [43b]) to IP wave transport. As we follow the shock to larger r, the ambient wave intensity falls at constant k but rises at constant k/B because $B \propto r^{-2}$. The radial variation of the ambient wave intensity at constant k/B is also manifested in the initial λ-r profiles shown in the top panels of Figure 2. A small damping rate ζ_1 has been introduced to moderate this effect (eqs. [19] and [42a]).

At fixed r ahead of the shock, protons with $\mu P \gtrsim 500$ MV arrive earliest to amplify waves at $k/B \lesssim 2 \times 10^{-3}$ MV^{-1}. Then more protons with progressively lower μP arrive to amplify waves at higher k/B. The top panels of Figure 3 confirm this progression of increasing wave growth from low to high k/B, peaking at $k/B \sim 2 \times 10^{-2}$ MV^{-1}. They also show that wave amplification diminishes quickly with r, as we already knew from the λ-r profiles in Figure 1. The wave growth rate γ_σ (eq. [19]) and the wave growth fall quickly with r because $V_{\rm A} \propto r^{-1}$ and the maximum value of $\partial f_{\rm H}/\partial\mu$ also falls quickly with r, a consequence of the temporal maximum of $f_{\rm H} \propto r^{-3}$ and the decreasing magnetic focusing strength.

The left-hand polarized Alfvén wave intensity I^{L+} is amplified by $\partial f_{\rm H}/\partial\mu > 0$ at $\mu < 0$. Thus, its growth must await the μ diffusion of the energetic protons from $\mu > 0$ and lags slightly the growth of I^{R+}. It is nevertheless amplified to about the same level as I^{R+} and shows similar characteristics and evolution. For brevity, its spectral evolution is not displayed.

At fixed r and k/B, there is an intriguing rapid decay from maximum wave intensity to the ambient level, leading to an apparent continuous sliding of the wave spectrum to the right (Fig. 3, *top panels*), the effect being faster and more prominent at smaller r. This feature may be understood by considering the effects of wave transport in (r, k/B)-space. First, the $R+$ waves travel outward at velocity $V_{\sigma f} = V_{\rm sw} + V_{\rm A}$, so that at a fixed r, one samples waves coming from progressively smaller values of r. Second, because $V_{\sigma f}$ decreases with r, as the wave packets travel outward, their wavenumbers k increase (eq. [15]). Third, because $B \propto r^{-2}$, these waves "see" a fast decreasing B and their k/B rises. Both the second and the dominant third effects transport the wave spectrum to higher k/B as the waves propagate outward. Therefore, at a fixed r, one samples at later time amplified waves that come from smaller r and that have moved to higher k/B (recall that wave amplification is stronger closer to the Sun). Finally, when the last

[4] We show our model results at $r = 1.15$ AU instead of 1 AU to compensate for the use of a radial instead of the Parker magnetic field.

amplified waves travel past, "fresh" waves emitted from the Sun at $t > 0$ arrive to return the wave spectrum to its original state. This is easily seen from the evolving λ-r profiles in the top panels of Figure 2. Far downstream of the shock, the nearly isotropic SEPs do not amplify the fresh waves significantly. The evolving I^{R+} spectrum (Fig. 3, *top panels*) and I^{L+} spectrum at $r = 0.35$, 0.75, and 1.15 AU account for the evolution of λ-P at the same r (Fig. 3 *bottom panels*).

We have seen in Figures 1 and 2 the powerful influence of the evolving Alfvén wave distributions on the SEPs and in Figures 3 and 4 the strong SEP excitation of the Alfvén waves in the inner heliosphere. In the next section we will examine more closely the coupling of the evolutions of SEP and Alfvén wave distributions via resonant interaction.

4.5. *Resonant Wave-Particle Interaction*

For simplicity, we will use QLT to interpret wave-particle interaction. It provides pretty good guidance despite the presence of some resonance broadening in our simulation. Equation (25) relates the μP of the SEPs and the k/B of the Alfvén waves in cyclotron resonance. It may be approximated by $k/B \approx (\mu P)^{-1}$. All panels of wave spectra shown in Figures 3 and 4 are marked with four vertical lines giving, from left to right, the k/B values of Alfvén waves in cyclotron resonance with 2.6 MeV amu^{-1} and $\mu = 1$ ions of $Fe^{+13.9}$ (279 MV), $O^{+6.67}$ (166 MV), He^{+2} (139.6 MV), and H^{+} (69.8 MV), respectively. At the same fixed energy per amu, with decreasing μ the resonant wavenumbers move to the right of the marked vertical lines and spread over broader bands of k/B because of resonance broadening. For Alfvén wave spectra with sign-inclusive power-law index $-\delta$, applying the quasilinear resonance function (eq. [7]) to the expression for the pitch-angle diffusion coefficient $D_{\mu\mu}$ (eq. [6]) yields the approximate relation

$$\frac{D_{\mu\mu}}{v} \propto P^{-2} \sum_{\sigma} I^{\sigma}(k_{\rm res}) \propto P^{\delta-2} , \qquad (59)$$

where $k_{\rm res}$ is given by equation (25). Thus, $D_{\mu\mu}/v$ increases with P if $\delta > 2$ (softer wave spectrum) and decreases with P if $\delta < 2$ (harder wave spectrum). For comparison with the displayed wave spectra, a line of slope $-\delta = -2$ is drawn in the top right corner of all panels of wave spectra in Figures 3 and 4 to aid the eye.

The top left panel of Figure 3 illustrates, at $r = 0.35$ AU and from $t = 0$ to $t \lesssim 12$ hr, the increasing distortion of the SEP-amplified wave spectrum from the initial Kolmogorov spectrum to possess increasingly large positive slope in the wavenumber range resonant with 2.6 MeV amu^{-1} $O^{+6.67}$ and $Fe^{+13.9}$ ions at $\mu \gtrsim \frac{1}{2}$. Thus, as discussed earlier in terms of the evolution of λ-P and λ-r profiles (Figs. 3 and 2), the transport of 2.6 MeV amu^{-1} $O^{+6.67}$ ions out of the inner heliosphere becomes so retarded relative to that of 2.6 MeV amu^{-1} $Fe^{+13.9}$ ions that the Fe/O ratio rebounds (Fig. 1, *bottom right panel*).

Of course, Fe/O must decrease again when $j^{\rm Fe}$ decays while $j^{\rm O}$ still rises. With increasing energy per amu, this wave growth–induced differential effect between $Fe^{+13.9}$ and $O^{+6.67}$ ions diminishes and the rebound disappears because the bulk of the resonant wavenumbers shift left to the unamplified Kolmogorov spectrum at $k/B \lesssim 2 \times 10^{-3}$ MV^{-1}. With decreasing energy, on the other hand, the resonant wavenumbers shift right to the steeper than k^{-2} part of the amplified wave spectrum at the relevant early time periods, and so at very low energies Fe/O rises from values less than 1.

In the earliest phase, when the SEP intensities are rising rapidly, the particles arriving at 1.15 AU have stayed essentially in the forward cone at $\mu \gtrsim 0.5$. The earliest minor ions travel through regions in which the resonant waves contributing to their $D_{\mu\mu}$ at $\mu \gtrsim 0.5$ have been amplified earlier by the passage of faster protons with similar μP values. However, comparison of the early wave spectra and particle mean free paths upstream of the shock reveals a subtle effect: the resonant waves have grown, but there is no apparent drop in the mean free paths. The resolution of this apparent paradox is as follows. The mean free path $\lambda = \frac{3}{8} \int_{-1}^{1} d\mu (1-\mu^2)^2 v/D_{\mu\mu}$ (Earl 1974) is a weighted average of $2v/(5D_{\mu\mu})$ over the full μ range, with the largest weight at $\mu = 0$. At early time, $D_{\mu\mu}$ increases only at $\mu \gtrsim 0.5$ and so produces little increase in the integral. In other words, in the early phase, the spatial diffusion concept is inapplicable and λ is not a good proxy for $D_{\mu\mu}$ at $\mu \gtrsim 0.5$. We have to go directly to the wave spectrum for clues on particle transport.

Comparing the two right-hand panels of Figure 1, we see that at 2.6 MeV amu^{-1}, Fe/O is larger than He/H near onset by greater than an order of magnitude, much larger than expected since $\lambda_{\rm Fe}/\lambda_{\rm O}$ is comparable to $\lambda_{\rm He}/\lambda_{\rm H}$ in the initial wave spectrum (Appendix C). To investigate this difference, we display in Figure 5 the evolution of the I^{R+} spectrum from $t \approx r/v$ to $t \approx 2r/v$ with $v = 0.535$ AU hr^{-1} at $r = 0.10$, 0.15, and 0.35 AU. During these intervals the 2.6 MeV amu^{-1} SEP intensities rise steeply and most SEPs arrive with $\mu > \frac{1}{2}$ as a result of scattering. To compare approximately the pitch-angle scattering rates of the ions at $\mu = 1$, we select the wave spectra near the start of the intervals and use the marked vertical lines. To compare at $\mu = \frac{1}{2}$, we select the wave spectra near the end of the intervals and shift the marked vertical lines to the right by a factor of 2. With the help of the k^{-2} guide lines, we see that in all three panels of Figure 5, $Fe^{+13.9}$ encounters significantly less scattering than $O^{+6.7}$, which explains why Fe/O falls from $\gg 1$. In contrast, He^{+2} ions encounter more scattering than protons at $r = 0.10$ and 0.15 AU and thus propagate out more slowly than the protons. At $r = 0.35$ AU, He^{+2} ions are scattered less than protons at $\mu = 1$ but more than protons at $\mu = \frac{1}{2}$. At larger r, the earliest He^{+2} ions are scattered less than the earliest protons. It appears that the stronger scattering at $r \lesssim 0.35$ AU and the weaker scattering at $r \gtrsim 0.35$ AU compensate to produce an early He/H ratio of ≈ 1 at $r = 1.15$ AU. At the lowest energies, the earliest ions of all species see amplified resonant waves in the steep spectral region at high k/B (not shown); consequently, both Fe/O and He/H rise from less than 1, although He/H starts lower. At the highest energy, the resonant k/B of all ion species fall in the lowest wavenumber regime where wave growth is insignificant; consequently, both He/H and Fe/O fall from comparable values greater than 1.

4.6. *Energy Spectra of SEP Intensities and Abundance Ratios*

Figure 6 illustrates, at $r = 1.15$ AU and $t = 10$, 18, and 26 hr, the evolution of the energy spectra of proton, He^{+2}, $O^{+6.7}$, and $Fe^{+13.9}$ differential intensities (*top panels*) and the evolution of the spectra of He/H and Fe/O normalized

ratios (*bottom panels*). The effect of velocity dispersion is present only at the lowest energies in the proton intensity spectrum at $t = 10$ hr. Scattering by SEP-amplified Alfvén waves contributes chiefly to the rollover of the SEP intensity spectra at a few MeV amu^{-1} at $t = 10$ and 18 hr. As all intensities rise at low energies and decay at high energies, the rollover gives way to an inflection by $t = 26$ hr. The effect of wave growth is sensitively reflected in the energy dependence of the Fe/O and He/H ratios. Interestingly, Fe/O peaks at lower energy than He/H at all three epochs, consistent with $O^{+6.7}$ and $Fe^{+13.9}$ having lower energies per amu than proton and He^{+2}, respectively, at equal rigidity or equal resonant wavenumber. At $t = 10$ hr, Fe/O has a maximum of 6 at 2 MeV amu^{-1}, while He/H has a lower maximum of 2.5 at 6 MeV amu^{-1}. Both ratios are relatively stable in time at high energies but rise gradually at low energies. Both the Fe/O and He/H spectral peaks descend slightly and move to somewhat lower energies in time. To demonstrate that the proton-amplified waves are responsible for the abundance enhancement from $\sim$0.5 to $\sim$10 MeV amu^{-1} but have little to do with the falling Fe/O and He/H spectra at high energy (other than the expected fall to slightly less than unity), we show the Fe/O and He/H source ratio spectra (also normalized to the coronal values) at $t = 0$ in the bottom panels of Figure 6.

With suitable choice of parameters, this model has been fitted to the observed evolving energy spectra of protons, He, O, and Fe intensities and the Fe/O and He/H time histories at $\sim$2.5 MeV amu^{-1} in the 1998 September 30 and 2000 April 4 gradual SEP events (Ng et al. 2001). The Fe/O spectral form shown in Figure 6 is similar to the Fe/C spectrum reported by Tylka et al. (2001) for the 2000 July 14 event except at $\gtrsim$30 MeV amu^{-1} where the observed upturn is attributed by these authors to shock acceleration of remnant flare suprathermals.

4.7. *SEP Anisotropies*

It is interesting to compare the anisotropies of the various ion species as a function of time and energy. For this purpose we characterize the anisotropies of energetic s-ions by the front-to-back ratios ζ_s of the phase-space distributions f_s (or differential intensities j_s), where

$$\zeta_s = \frac{\int_{0.65}^{1} f_s \, d\mu}{\int_{-1}^{-0.65} f_s \, d\mu} = \frac{\int_{0.65}^{1} j_s \, d\mu}{\int_{-1}^{-0.65} j_s \, d\mu} \ . \tag{60}$$

Note that these are the front-to-back ratios in the solar wind frame. Figure 7 shows, in the left-hand and middle panels, the time histories at $r = 1.15$ AU of ζ_H, ζ_{He}, ζ_O, and ζ_{Fe} at 1.30, 2.59, 5.18, and 10.33 MeV amu^{-1}. For all species, ζ decreases with energy and generally decays with time, except for shoulders around 15 hr at 1.30 MeV amu^{-1} for the minor ions. As we go to higher A/Q species, the variation of ζ over the fixed energy range expands, suggesting an association with the broader rigidity range spanned by higher A/Q species.

To compare the front-to-back ratios of neighboring species, we have evaluated the time histories of ζ_H/ζ_{He} and ζ_O/ζ_{Fe}, displayed in the right-hand panels of Figure 7. At the higher energies ζ_O/ζ_{Fe} and ζ_H/ζ_{He} rise and cross from less than 1 to greater than 1. This crossing occurs earlier at higher energy per amu. The ratio ζ_O/ζ_{Fe} crosses earlier to higher values than ζ_H/ζ_{He} at the same energy per amu. What are the reasons for the above interesting features?

At very early time, since $Fe^{+13.9}$ ions are scattered less than $O^{+6.7}$ ions (an effect enhanced by proton-amplified waves), the $Fe^{+13.9}$ pitch-angle distribution broadens more slowly than that of $O^{+6.7}$ ions. Thus, the early ζ_O/ζ_{Fe} is less than 1, similarly for ζ_H/ζ_{He}. What then causes the rise above unity? In this simulation, a partially (95%) reflecting outer boundary expands outward from $r = 2$ AU at the solar wind velocity of 0.008 AU hr^{-1}. Because $Fe^{+13.9}$ ions are scattered less than $O^{+6.7}$ ions, $Fe^{+13.9}$ ions are more likely to travel to this moving outer boundary at $r \gtrsim 2$ AU and return to $r = 1.15$ AU than $O^{+6.7}$ ions of equal energy per amu. Thus, ζ_{Fe} decays faster and falls below ζ_O so that ζ_O/ζ_{Fe} rises above unity. Similar consideration applies to He^{+2} and protons, with the addition that the return takes longer because of the greater scattering of protons and He^{+2} ions than $O^{+6.7}$ and $Fe^{+13.9}$ ions at equal energy per amu.

In a study comparing Fe/O ratios in the sunward and antisunward hemispheres in SEP events observed on the *Wind* spacecraft (Reames & Ng 2002), it was discovered that sunward Fe/O is greater than antisunward Fe/O by a factor of 1.15–1.53, equivalently, $\zeta_O/\zeta_{Fe} = 1.15$–1.53, similar to those shown in the bottom right panel of Figure 7. No event was observed in which antisunward Fe/O dominates. The current model is able to match the observations with the partially reflecting boundary placed at $r \lesssim 1.8$ AU. It should be pointed out that with $\lambda_{Fe} > \lambda_O$, the classical diffusion model in an infinite medium predicts $\zeta_O/\zeta_{Fe} = 1$ for an impulsive point source and $\zeta_O/\zeta_{Fe} < 1$ for a time-extended source. With $\lambda \gtrsim 0.1$ AU and $V_{sw} = 400$ km s^{-1}, the Fisk & Axford (1968) convection diffusion model in an infinite medium predicts that $Fe^{+13.9}$ anisotropy exceeds $O^{+6.7}$ anisotropy by less than 5×10^{-3} at $t \gg 16$ hr, too small and too late to match the observations. Taken together, the above contrasting predictions indicate the existence of a region that strongly scatters or magnetically reflects the SEPs at varying distance beyond the Earth's orbit. Such regions are known to exist as corotating interaction regions produced by stream-stream interaction, as enhanced turbulence and magnetic field enhancement near CME-driven IP shocks (e.g., Bieber et al. 2002), or simply as magnetic bottles from CMEs (Reames 2002). The influence of such regions is crudely modeled here via a partially reflecting boundary.

4.8. *SEP Source from a Stronger Shock*

We now consider case 2, for SEP injection spectra extending to higher energies and staying hard longer than in case 1, by changing three parameters relating to the shock-accelerated particle source. The initial e-folding energy $E_{e,0}$ is increased from 60 to 2000 MeV, the rate of spectral steepening α' is decreased from 2.5 to 0.5 AU^{-1}, and the seed particle fraction b is decreased from 5×10^{-3} to 2.5×10^{-3} (see Table 1). For case 2, we display in Figures 8 and 9 the calculated time histories and the energy spectra at selected epochs of the proton, He, O, and Fe intensities and the He/H and Fe/O ratios at $r = 1.15$ AU, for comparison with the corresponding plots in Figures 1 and 6 of case 1. We also show, in Figure 10, the I^{R+} wave spectra at fixed r and at locations comoving with the shock, to be compared with Figure 3 (*top panels*) and Figure 4 of case 1.

Comparison of Figures 1 and 8 shows that in case 2, the early particle intensities, especially j^{Fe}, tend to be lower,

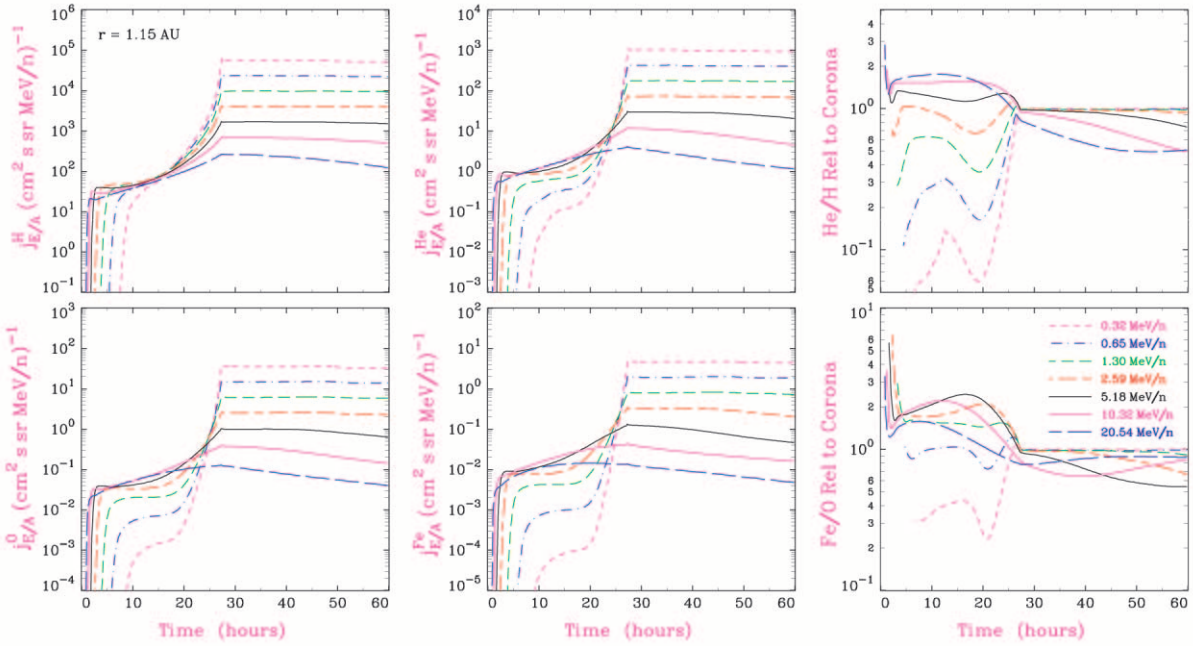

FIG. 8.—As in Fig. 1, but for case 2

although they eventually rise to much larger values at shock arrival. The He/H and Fe/O ratios in case 2 exhibit quite different time variations than those in case 1. In case 2, both Fe/O and He/H do not rise as high as in case 1, and Fe/O at $E/A \lesssim 650$ keV amu^{-1} and He/H at $E/A \lesssim 2.6$ MeV amu^{-1} dip before rising to near coronal value at shock crossing. These differences may be traced to the different amplified wave distributions in the two cases. For example, comparing the I^{R+} spectra at $s = 0.05$ AU upstream of the shock (Figs. 4 and 10), we see that the spectral slope at $k/B \gtrsim 3 \times 10^{-2}$ MV^{-1} hardens past -2 at $t \approx 18$ hr in case 1 but much later at $t \approx 36$ hr in case 2 (shock passage is at $t \approx 28$ hr). This means that, prior to such times at $P \lesssim 30$ MV, low-A/Q ions "escape" more easily than high A/Q ions from the shock, hence the rise of He/H and Fe/O at corresponding energies from below coronal to coronal

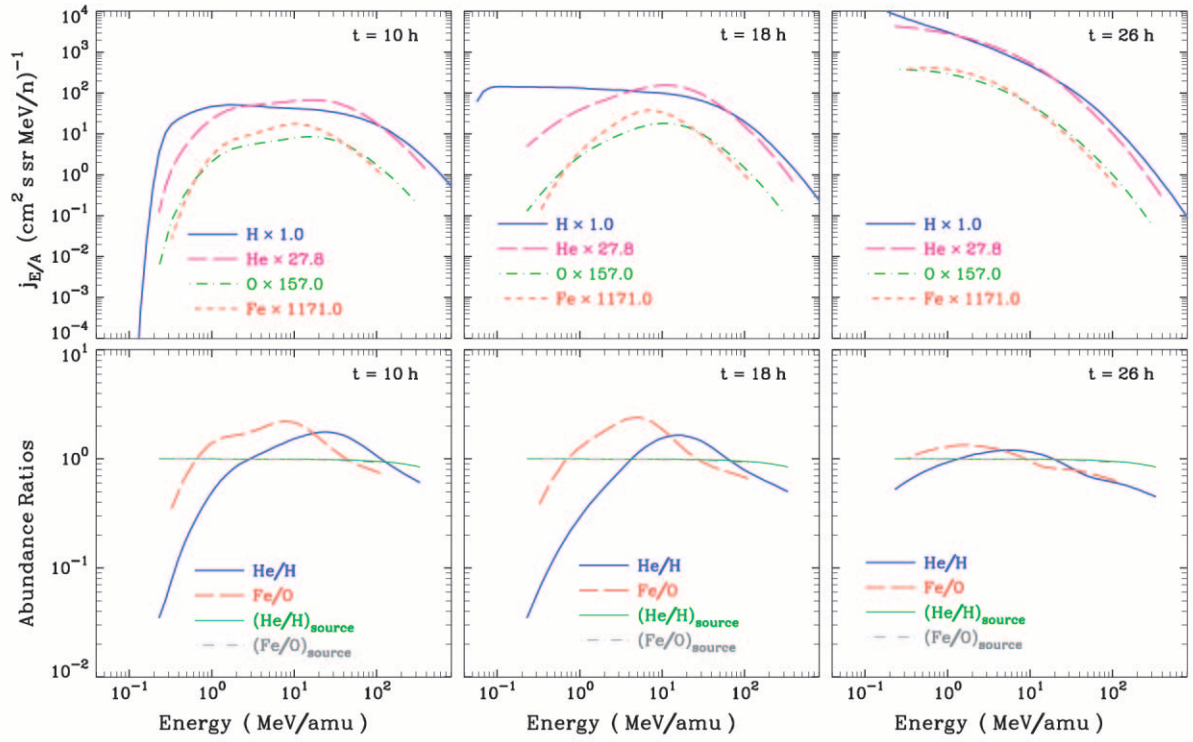

FIG. 9.—*Top panels*: As in Fig. 6, but for case 2

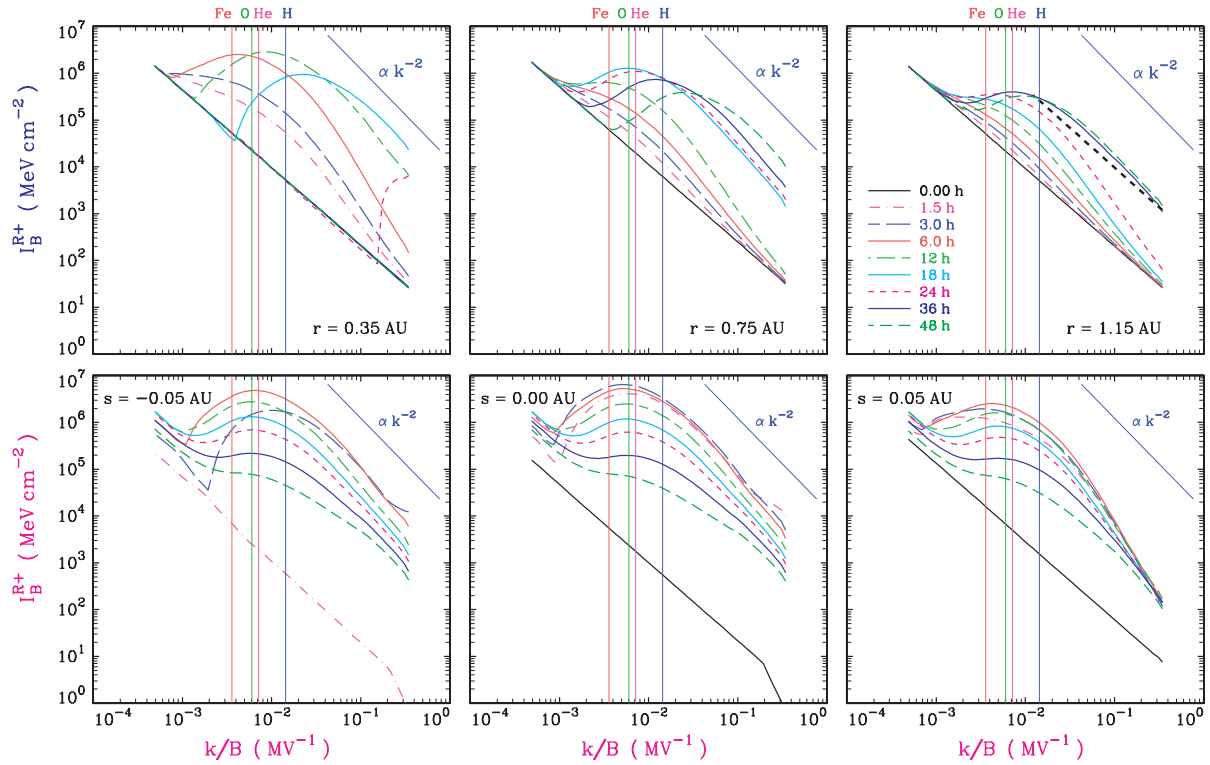

FIG. 10.—For case 2: time evolution of I^{R+} spectrum at $r = 0.35$, 0.75, and 1.15 AU (*top panels*), and at $s = -0.05$, 0, and 0.05 AU upstream from the traveling shock (*bottom panels*). The vertical lines give, from left to right, the resonant wavenumbers for 2.6 MeV amu^{-1} $Fe^{+13.9}$, $O^{+6.7}$, He^{+2}, and H^{+} ions at $\mu = 1$. At $r = 1.15$ AU, the I^{R+} spectrum peaks near shock crossing at $t = 28$ hr and barely exceeds the magnetic power spectrum observed by Leamon et al. (1998) (*thick black dashed line in the top right panel*) at $k/B \gtrsim 1.5 \times 10^{-2}$ MV^{-1}.

values as the shock approaches. Similarly, we may relate the lower rebounds of Fe/O and He/H at high energies in case 2 to the smaller positive slopes of the various wave spectra at $k/B \lesssim 8 \times 10^{-3}$ MV^{-1} in case 2 (despite the much higher wave intensities).

In both cases 1 and 2, the He/H and Fe/O energy spectra are dominated at high energies by the (different) energy spectra of the respective source ratios (Figs. 6 and 9). The proton-driven wave growth is much stronger in case 2. Nevertheless, as shown in the top right panel of Figure 10, the I^{R+} spectrum at $r = 1.15$ AU barely rises above the magnetic field power spectrum evaluated by Leamon et al. (1998) at $k/B \gtrsim 1.5 \times 10^{-2}$ MV^{-1}.

4.9. *Maximum Wave Growth Rate and Wave Energy Density*

The quasilinear theory underlying the wave growth rate (eq. [19]) and the particle pitch-angle diffusion coefficient (eq. [6]) assumes that $\gamma_\sigma/\omega \ll 1$ and $\langle(\delta B)^2\rangle/B^2 \ll 1$. In view of the strong and rapid wave growth in the simulations, we now examine whether these assumptions are satisfied.

The wave growth rate is largest just upstream of the moving shock, peaks early in time, and then decreases rapidly as the shock propagates outward. In case 1, the maximum wave energy growth rate $\gamma_{R+} = 100$ hr^{-1} occurs at $t = 0.08$ hr, $k/B = 4.34 \times 10^{-2}$ MV^{-1}, and $r = 0.075$ AU, where $B = 605$ nT and $V_A = 1.07 \times 10^{-2}$ AU hr^{-1}. Thus, $\omega = 1.26 \times 10^4$ hr^{-1} and the proton cyclotron frequency $\Omega_p = 2.09 \times 10^5$ hr^{-1}. This gives $\gamma_{R+}/\omega = 8.0 \times 10^{-3}$ and $\omega/\Omega_p = 6.0 \times 10^{-2}$. For case 2, the maximum $\gamma_{R+} = 73$ hr^{-1} occurs at $t = 0.10$ hr, $k/B = 4.87 \times 10^{-2}$ MV^{-1}, and $r = 0.075$ AU, giving $\gamma_{R+}/\omega = 5.2 \times 10^{-3}$ and $\omega/\Omega_p = 6.8 \times 10^{-2}$. Thus, in both cases 1 and 2, the maximum wave growth rate is very large but remains small relative to the wave angular frequency and proton cyclotron frequency.

Examining the wave spectra, we find that in both cases 1 and 2, I^{R+} and I^{L+} peak at $t \approx 1.5$ hr and at the shock ($r_{sh} \approx 0.125$ AU). In case 1, the maximum wave magnetic energy density $\langle(\delta B)^2\rangle/(8\pi) = \int (I^{R+} + I^{L+})dk/(8\pi) = 3.2 \times 10^{-3}$ MeV cm^{-3}, with the bulk of the wave energy residing in the interval 6×10^{-3} MV$^{-1} \lesssim k/B \lesssim 0.1$ MV^{-1}. The mean magnetic field of 218 nT gives $B^2/(8\pi) = 0.118$ MeV cm^{-3}, and so $\langle(\delta B)^2\rangle/B^2 = 0.027$. In case 2, the stronger and harder proton source produces a higher maximum wave magnetic energy density of 4.4×10^{-3} MeV cm^{-3}, and $\langle(\delta B)^2\rangle/B^2 = 0.037$. The injection of higher energy protons causes the bulk of the amplified wave energy to reside in the lower wavenumber range from 3×10^{-3} to 8.7×10^{-2} MV^{-1}.

While the wave energy density $B^2/(8\pi)$ at the shock peaks early close to the Sun, the ratio $\langle(\delta B)^2\rangle/B^2$ at the shock increases with r_{sh} from less than 0.004 early in the event to peak at $\approx$0.08 (0.43) when $r_{sh} \approx 0.3$ AU (0.75 AU) in case 1 (2) and then decreases farther out. Thus, the assumption of $\langle(\delta B)^2\rangle/B^2 \ll 1$ is generally satisfied, especially when the wave energy density is high early in the event. The radial dependence of $\langle(\delta B)^2\rangle/B^2$ at the shock may be traced to the similar radial dependence in the ratio of the ambient wave energy density to the mean magnetic field energy density.

It may come as a surprise that the assumptions are well satisfied where the growth rate is largest and where the wave intensity is highest, respectively. However, the maximum growth rate and maximum wave intensity occur near the Sun, where B, Ω_p, and V_A are large compared to their values at $r = 1$ AU. Furthermore, wave growth is a self-throttling process: fast wave growth quickly produces more pitch-angle scattering to reduce proton streaming.

Finally, it is important to note that the solutions for SEP distributions f_s and wave intensities I^σ versus k/B are invariant under the parameter transformation:

$$n_{s,0} \rightarrow \beta n_{s,0}, b \rightarrow \beta^{-1} b, B_0 \rightarrow \beta^{1/2} B_0 \ , \qquad (61)$$

with β a positive constant, all other parameters listed in Table 1 being unchanged. This means that a single computation solves not one model but a family of models. B_0 is actually not an independent parameter in Table 1, and the third member in the transformation given by equation (61) is dictated by the first and a fixed $V_{A,0}$. The transformation preserves the product bn_s. Since $V_{A,0}$ and η_0 are fixed, it implies the derived transformations $B \rightarrow \beta^{1/2} B$, $k \rightarrow \beta^{1/2} k$, and $\langle (\delta B)^2 \rangle / B^2 \rightarrow \beta^{-1/2} \langle (\delta B)^2 \rangle / B^2$. For example, starting from the parameters in Table 1 and the implied $B_0 = 3.41$ nT, we obtain with $\beta = 2$ a new model with $n_{H,0} = 10\ \mathrm{cm}^{-3}$, $B_0 = 5$ nT, and $b = 2.5 \times 10^{-3}$ (case 1) or 1.25×10^{-3} (case 2), to which all the results on $j_{E/A}$ and I^σ versus k/B for case 1 or case 2 apply, but the new value of $\langle (\delta B)^2 \rangle / B^2$ is smaller by the factor $2^{-1/2}$. The observed power spectrum shown in Figures 3 and 10 is unaffected by this transformation.

5. SUMMARY AND DISCUSSION

Energy conservation requires that scattering of streaming SEPs by IP Alfvén waves must go hand in hand with wave amplification by the SEPs (Appendix B). Therefore, in adopting wave-particle interaction as the physical basis for SEP scattering with the related pitch-angle scattering coefficient $D_{\mu\mu}$ or mean free path λ, we must also take account of wave growth with the wave growth rate γ_σ. We have taken this step in modeling gradual SEP events. Based on quasilinear wave-particle interaction augmented with resonance broadening, and with reasonable IP and shock parameters (Table 1), our model demonstrates that in gradual SEP events the self-amplified waves indeed play an essential role in a novel mode of SEP transport. The quasilinear assumptions are confirmed a posteriori: the maximum wave growth rates obtained, although very large ($\sim$100 hr^{-1}), are small relative to the wave frequency, and the maximum wave spectra satisfy $\langle (\delta B)^2 \rangle / B^2 \ll 1$.

The model simulates the coupled evolution of the phase-space distributions $f_s(\mu, P, r, t)$ of shock-accelerated SEPs and the spectral magnetic intensities $I^\sigma(k, r, t)$ of IP Alfvén waves, taking account of the pitch-angle scattering of SEPs by Alfvén waves and the associated wave amplification by streaming SEPs, magnetic focusing in the IMF, convection with the solar wind, adiabatic deceleration, a moving source of multispecies shock-accelerated SEPs, and WKB transport of Alfvén waves.

For shock-accelerated SEP source spectra with proton e-folding energy $E_e = 60$ MeV and fast softening (Table 1, case 1), we presented various aspects of the simulated SEP and Alfvén wave distributions: time histories of the intensities $j_{E/A}$, abundance ratios, and anisotropies of protons, He, O, and Fe ions; radial profiles of $j_{E/A}$ and mean free paths λ; energy spectra of $j_{E/A}$ and abundance ratios; and Alfvén wave spectra at fixed r and at locations comoving with the shock. For contrast, SEP intensity time histories and spectra, as well as wave intensity spectra, are also presented for SEP source spectra that stay hard longer and with $E_e = 2000$ MeV (Table 1, case 2). The different magnitudes and spectral forms of the proton-amplified IP Alfvén waves play a major role in producing the significantly different time variations and energy spectra of He/H and Fe/O in cases 1 and 2.

A graphic illustration of the powerful control exerted by the proton-amplified waves on the species-dependent transport of SEPs is given in Figure 2: the concurrent snapshots of $j_{E/A}$-r and λ-r profiles demonstrate vividly the retardation of outward SEP transport by the moving region of amplified waves, producing flat intensity profiles behind and steep profiles in and ahead of this region. Similarly, juxtaposing the λ-P profiles and I^{R+}-k/B spectra shows clearly how the evolving wave spectra dynamically shape and alter the dependence of λ on P and on ionic species (Fig. 3). Via the resonance condition $k/B \approx (|\mu| P)^{-1}$, we see how the evolving wave spectra and λ-P profiles (Figs. 3 and 4) affect the Fe/O and He/H time histories (Fig. 1). Examination of the local wave spectra following the motion of the earliest SEPs confirms that the early amplified wave spectra are responsible for the difference in the onset ratios of He/H and Fe/O at equal energy per amu (Fig. 5).

Although proton streaming is responsible for wave amplification, outward wave transport (including solar wind convection) also plays an important role in SEP transport. As the amplified waves, absent at low k/B as a result of the proton spectral cutoff at high P, travel outward into weaker magnetic field, they simultaneously move to higher k/B and resonate with lower rigidity ions with $|\mu| P \approx (k/B)^{-1}$. Thus, high-rigidity ions "free" themselves from the amplified waves earlier than low-rigidity ions.

The early amplified wave spectra at small distances upstream of the shock are much steeper than k^{-2} at $k/B \gtrsim 2 \times 10^{-2}$ MV^{-1} (Figs. 4 and 10), implying that $D_{\mu\mu}$ *increases* with P at $|\mu| P \lesssim 50$ MV. For a finite-time shock, this appears to imply, interestingly, that high-A/Q ions (e.g., Fe^{+14}) are more quickly accelerated to $|\mu| P \sim 50$ MV than low-A/Q ions (e.g., O^{+7}). Although only a model that treats shock acceleration and transport of SEPs coupled self-consistently to wave evolution can confirm this suggestion, we may speculate that via the self-amplified waves the shock acceleration process itself may enhance the Fe/O ratio above the coronal value early in the event.

Thermal, cyclotron, and other damping processes at $k V_A / \Omega_p \gtrsim \frac{1}{2}$ should limit the maximum wave intensity at small r and produce spectral slope steeper than k^{-2} (e.g., Gary 1993; Bieber et al. 1994; Leamon et al. 1998). We have taken account of this heuristically by introducing a high-wavenumber cutoff, but we have not included in this paper the strong damping effect at the high wavenumbers (which would give less scattering than predicted for low-rigidity particles at small r). We explored the effects of nonlinear wave cascading that result from the interaction of inward- and outward-propagating waves (Zhou & Matthaeus 1990; Tu & Marsch 1990). However, the cascade rate does not increase with the growth of the outward waves because the streaming protons also damp the inward waves strongly. Consequently, the effect of nonlinear cascading is probably

small compared to that due to wave propagation into rapidly decreasing IMF discussed above. We do not include wave cascading in the current model.

In gradual SEP events, shock acceleration and transport of SEPs occur concurrently with wave evolution and shock propagation in finite time. This complex dynamic situation involving all four processes poses a severe challenge, in view of the strong spatial variation of plasma parameters that the shock goes through in a short time (Lee 2000). The assumed shock propagation and decoupling of acceleration and transport in our model are quite clearly an oversimplification. Within the limitation of this approach, we try to include heuristically various features of shock acceleration in the SEP source term (eq. [8]). The shock-accelerated ion source spectra have the form of a rigidity power law times an A/Q-dependent exponential factor (Ellison & Ramaty 1985) and involve various IP and shock parameters listed in Table 1, viz., $V_{\rm sw}$, $n_{\rm H,0}$, $V_{\rm sh}$, $r_{\rm sh,0}$, E_0/A, b, α_0, α', $E_{e,0}$, and the charge states of the minor ions. The power-law spectral index α approximates that of the steady state shock spectrum (e.g., Lee 1983), and the r variation of the e-folding energy E_e (eq. [12]) parallels that of the maximum particle energy in the Zank et al. (2000) acceleration model. The model parameters relevant to the IP Alfvén waves are $V_{\rm A,0}$, $I^{\sigma 0}$, η_0, δ, and ζ_1 (see Table 1).

In any gradual SEP event, $n_{\rm H,0}$, $V_{\rm A,0}$, $V_{\rm sw}$, $r_{\rm sh,0}$, and $V_{\rm sh}$ are measured quantities. The minor-ion number densities $n_{s,0}$ are fixed relative to $n_{\rm H,0}$ through known coronal abundances (Reames 1999). The ambient Alfvén wave magnetic intensity spectra $I^{\sigma 0}$ at 1 AU are in principle also measurable, but they are not simply related to the much larger measured IMF power spectra owing to the presence of other sources of fluctuations. E_0/A is usually taken to be the energy per amu of the solar wind suprathermal particles ($\sim$5 keV amu^{-1}), and that is followed in this paper. However, if the seed particles derive from a small reflected fraction of the solar wind flux into the shock, then $E_0 \approx 2m_p(V_{\rm sh} - V_{\rm sw})^2$ and may significantly shorten the first-order Fermi acceleration time to high energies. This is also true if the seed particles originate in remnants from previous SEP events (Mason, Mazur, & Dwyer 1999; Desai et al. 2001; Tylka et al. 2001). The parameters b, E_0, α, α', and $E_{e,0}$ relating to the accelerated particle spectra are present because the model does not treat shock evolution and particle acceleration explicitly. The combination in which they appear in the source term (eq. [8]) would generally be well constrained by the observed SEP intensity spectra. The charge states of the minor ions are measured at less than 1 MeV amu^{-1} by *ACE*/SEPICA (Möbius et al. 2002) and up to $\sim$40 MeV amu^{-1} in some events by SAMPEX (Mazur et al. 1999). The Fe charge state appears to increase with energy (Möbius et al. 2002). If the SEPs are shock accelerated from the solar wind suprathermals, the charge states may be taken to be those measured in the solar wind. On the other hand, if shock acceleration begins at low coronal heights so that the product of the electron number density and coronal residence time is $\gtrsim 3 \times 10^9$ cm^{-3} s, then the minor-ion charge states would vary during acceleration (Ruffolo 1997; Reames et al. 1999; Barghouty & Mewaldt 2000; Ostryakov et al. 2000), a scenario not considered in our model.

The inner boundary radius r_a is not a free parameter. It certainly has to be less than $r_{\rm sh,0}$, which is $\sim$2–4 $R_\odot$ (Kahler 1994). We have chosen $r_a = 10.7\ R_\odot$ to be consistent with the assumed simple r dependence of n_s, $V_{\rm A}$, and the implied B and also to reduce the time of computation. The model results at 1 AU do not vary significantly with r_a from 10.7 to 16 $R_\odot$. The outer boundary radius r_b and the reflection coefficient $\alpha_{\rm refl}$ relate to a disturbed region such as a shock or stream-stream interaction region behind 1 AU, in principle observable (e.g., Bieber et al. 2002). The resonance broadening factor $a = 0.10$ has been chosen to bridge the resonance gap but not to produce too much scattering. The results presented are not sensitive to a in the range 0.05–0.15; although at $a = 0.05$, protons below 200 keV exhibit near–scatter-free behavior. To moderate the steep r dependence in λ implied by the undamped steady state WKB ambient wave distributions, we introduced the small wave damping rate $\zeta_1 = -0.01$ hr^{-1}, adopted from Bavassano et al. (1982), to allow a slow IP damping. It has little effect on the dynamic wave evolution, which is dominated by the effect of SEP streaming.

The physical processes included in our model naturally require the specification of the related IP and shock parameters (Table 1). Most of these are directly observable in practice or in principle. The others are constrained by SEP observation. We note that the wave growth rate increases with the Alfvén speed (eq. [19]), which has been observed to vary considerably. The model or its predecessor was successfully fitted to the study of the concurrent time histories and energy spectra of multispecies SEP intensities and the abundance ratios in the 1998 April 20, 1998 September 30, and 2000 April 4 gradual SEP events (Ng et al. 1999a, 2001; Tylka 2001). Proton-driven wave amplification was also found to be consistent with the observational studies comparing the SEP abundance ratios of large versus small and hard versus soft gradual SEP events (Reames et al. 2000) and with the observational study on SEP anisotropies (Reames et al. 2001). We believe that the model provides a credible account of the effects of SEP transport through self-amplified waves, which must also be taken into account in future efforts to understand the process of shock acceleration itself.

We thank S. P. Gary for discussion on wave damping and the referee for valuable comments. This work is supported by NASA LWS 784-50-00-08. A. J. T. was supported by the Office of Naval Research and NASA DPR S-13791-G.

APPENDIX A

RESONANCE FUNCTION

In this paper $R^{\sigma}_{\mu\mu}$, the resonance function due to σ-mode Alfvén waves, denotes the quantity $\langle(1-\mu^2)R^{\sigma 1}_{\mu\mu}\rangle$ in Ng & Reames (1995). We approximate it by the closed form below:

$$R^{\sigma}_{\mu\mu} = 2\pi\left(1-\frac{\mu V_\sigma}{v}\right)^2 \frac{1-\acute{\mu}^2}{kv}\frac{1}{\sqrt{2\pi}\chi}\exp\left[-\frac{1}{2\chi^2}\left(\mu-\frac{V_\sigma}{v}-\frac{g_\sigma\Omega}{k\gamma v}\right)^2\right], \tag{A1}$$

$$\chi = \sqrt{2}a_0\left(1-\acute{\mu}^2\right)^{1/2}, \tag{A2}$$

$$1-\acute{\mu}^2 = \left(1-\mu^2\right)\left(1-\tfrac{1}{2}a_0^2\right)+a_0^2\mu^2 . \tag{A3}$$

We have restricted the wavenumber k to positive values, hence the presence of g_σ in equation (A1), where for $B>0$, $g_\sigma = 1$ for $\sigma = R^+, L^-$, and $g_\sigma = -1$ for $\sigma = R^-, L^+$. The parameter a_0 determines the strength of resonance broadening, $V_\sigma = \pm V_A$, Ω is the ion angular cyclotron frequency, and γ is the Lorentz factor. Note that $\Omega/(\gamma v) = B/P = QeB/(Am_pc\gamma v)$. When the parameter $a_0 \to 0$, $1-\acute{\mu}^2 \to 1-\mu^2$, $\chi \to 0$, and we recover the quasilinear result

$$R^{\sigma}_{\mu\mu} \to 2\pi\left(1-\frac{\mu V_\sigma}{v}\right)^2\frac{1-\mu^2}{kv}\delta\left(\mu-\frac{V_\sigma}{v}-\frac{g_\sigma\Omega}{k\gamma v}\right). \tag{A4}$$

As a function of wavenumber k, $R^{\sigma}_{\mu\mu}$ has a peak at

$$k_{\max} = \frac{2\Omega}{\gamma v\Upsilon}, \tag{A5}$$

where

$$\Upsilon = g_\sigma\left(\mu-\frac{V_\sigma}{v}\right)+\left[\left(\mu-\frac{V_\sigma}{v}\right)^2+4\chi^2\right]^{1/2}, \tag{A6}$$

and

$$R^{\sigma}_{\mu\mu}(k_{\max}) = \sqrt{\frac{\pi}{2}}(1-\acute{\mu}^2)\left(1-\frac{\mu V_\sigma}{v}\right)^2\frac{\gamma\Upsilon}{\Omega\chi}\exp\left(-\frac{2\chi^2}{\Upsilon^2}\right). \tag{A7}$$

APPENDIX B

ENERGY CONSERVATION AND WAVE GROWTH RATES

In this appendix we use energy conservation to show that the particle transport equation (B1) with the general relation given by equation (B10) between the particle diffusion coefficient $D^{\sigma}_{\mu\mu}$ and the wave spectral magnetic intensity I^σ must imply the expression given by equation (B14) for the wave growth rate γ_σ of σ-mode Alfvén wave spectral energy density ($=2I^\sigma/8\pi$) in terms of the momentum gradients of the phase-space densities f_s of solar energetic ions. For a derivation from the plasma dispersion relation, see, e.g., Lee (1971, 1982) or Melrose (1980).

The transport equation for energetic s-ions in mixed coordinates (see eq. [5]) reads (e.g., Schlickeiser 1989a; Skilling 1975; Ruffolo 1995)

$$\begin{aligned}\frac{df_s}{dt} &\equiv \frac{\partial f_s}{\partial t}+(\mu v+V_{sw})\frac{\partial f_s}{\partial r}-\frac{1-\mu^2}{2B}\frac{dB}{dr}\left[(v+\mu V_{sw})\frac{\partial f_s}{\partial\mu}-V_{sw}p\frac{\partial f_s}{\partial p}\right]\\ &= \sum_\sigma\left\{\frac{\partial}{\partial\mu}\left[D^{\sigma}_{\mu\mu}\frac{\partial f_s}{\partial\mu}+\frac{\partial f_s}{\partial p}\right]+\frac{1}{p^2}\frac{\partial}{\partial p}\left[p^2\left(\frac{\partial f_s}{\partial\mu}+\frac{\partial f_s}{\partial p}\right)\right]\right\},\end{aligned} \tag{B1}$$

where the sum is over all relevant Alfvén wave modes. The momentum transport coefficients $D^{\sigma}_{\mu\mu}$, $D^{\sigma}_{\mu p} = D^{\sigma}_{p\mu}$, and D^{σ}_{pp} govern the diffusion of the ions in (μ, p)-space because of their interaction with the σ-mode Alfvén waves. Assuming that the σ-mode wave electric field vanishes in that wave frame moving with velocity V_σ relative to the plasma and the particles are pitch-angle

scattered but conserve their energies in that frame, these coefficients are related as follows:

$$D^{\sigma}_{\mu p} = D^{\sigma}_{p\mu} = g_{\sigma} p D^{\sigma}_{\mu\mu} \, , \tag{B2}$$

$$D^{\sigma}_{pp} = g_{\sigma} p D^{\sigma}_{\mu p} = g^2_{\sigma} p^2 D^{\sigma}_{\mu\mu} \, , \tag{B3}$$

$$g_{\sigma} = \left(\frac{V_{\sigma}}{v} \right) \left(1 - \frac{\mu V_{\sigma}}{v} \right)^{-1} \, . \tag{B4}$$

We may write equation (B1) as

$$\frac{df_s}{dt} = - \frac{\partial}{\partial \mu} \langle \dot{\mu}_s \rangle f_s - \frac{1}{p^2} \frac{\partial}{\partial p} \left(p^2 \langle \dot{p}_s \rangle f_s \right) \, , \tag{B5}$$

where $\langle \dot{\mu}_s \rangle$ and $\langle \dot{p}_s \rangle$ denote the mean time rate of change of the μ and p of the energetic s-ions, and identify

$$- \langle \dot{\mu}_s \rangle f_s = \sum_{\sigma} D^{\sigma}_{\mu\mu} \left(\frac{\partial f_s}{\partial \mu} + g_{\sigma} p \frac{\partial f_s}{\partial p} \right) = \sum_{\sigma} \frac{1}{1 - \mu V_{\sigma}/v} D^{\sigma}_{\mu\mu} G_{\sigma s} f_s \, , \tag{B6}$$

$$- \langle \dot{p}_s \rangle f_s = \sum_{\sigma} D^{\sigma}_{\mu p} \left(\frac{\partial f_s}{\partial \mu} + g_{\sigma} p \frac{\partial f_s}{\partial p} \right) = \sum_{\sigma} \frac{V_{\sigma}/v}{(1 - \mu V_{\sigma}/v)^2} p D^{\sigma}_{\mu\mu} G_{\sigma} f_s \, , \tag{B7}$$

where

$$G_{\sigma} f_s \equiv \frac{\partial f_s}{\partial \mu} - \frac{V_{\sigma}}{v} \left(\mu \frac{\partial f_s}{\partial \mu} - p \frac{\partial f_s}{\partial p} \right) \, . \tag{B8}$$

From equation (B7), we obtain $\langle \dot{E}_s \rangle$, the mean time rate of change of the s-ion energy:

$$\langle \dot{E}_s \rangle f_s = v \langle \dot{p}_s \rangle f_s = - \sum_{\sigma} \frac{V_{\sigma}}{(1 - \mu V_{\sigma}/v)^2} p D^{\sigma}_{\mu\mu} G_{\sigma} f_s \, . \tag{B9}$$

In the above equation, the pitch-cosine diffusion coefficient $D^{\sigma}_{\mu\mu}$ due to the σ-mode Alfvén waves may be expressed in terms of the wave spectral magnetic intensity I^{σ} (see eq. [6]):

$$D^{\sigma}_{\mu\mu}(\mu, v, P, r, t) = \frac{Q^2 e^2 v^2}{4 p^2 c^2} \sum_{\sigma} \int dk \, I^{\sigma}(k, r, t) R^{\sigma}_{\mu\mu}(\mu, v, P, k, V_{\sigma}, B) \, , \tag{B10}$$

leading to

$$\langle \dot{E}_s \rangle f_s = - \sum_{\sigma} \frac{V_{\sigma}}{(1 - \mu V_{\sigma}/v)^2} \frac{Q^2_s e^2 v^2}{4 p c^2} \int dk \, I^{\sigma}(k, r, t) R^{\sigma}_{\mu\mu} G_{\sigma} f_s \, . \tag{B11}$$

From the conservation of the total energy in all wave modes and all species of energetic ions, we have

$$\frac{\partial}{\partial t} \sum_{\sigma} \int dk \frac{2 I^{\sigma}}{8\pi} + \sum_{s} 2\pi \int\int d\mu \, dp \, p^2 \langle \dot{E}_s \rangle f_s = 0 \, . \tag{B12}$$

The wave spectral total energy density in the plasma rest frame is double the wave spectral magnetic energy density $I^{\sigma}/8\pi$, the wave electric energy density being negligible. From equations (B11) and (B12), we obtain

$$\sum_{\sigma} \int dk \left[\frac{2}{8\pi} \frac{\partial I^{\sigma}}{\partial t} - I^{\sigma} \sum_{s} 2\pi Q^2_s e^2 \int\int d\mu \, dp \, p^2 V_{\sigma} \frac{v^2}{4 p c^2} \frac{R^{\sigma}_{\mu\mu}}{(1 - \mu V_{\sigma}/v)^2} G_{\sigma} f_s \right] = 0 \, . \tag{B13}$$

Assuming that waves of different σ-modes and wavenumbers are uncorrelated, equation (B13) gives the growth rate $\gamma_{\sigma} \equiv (I^{\sigma})^{-1} \partial I^{\sigma}/\partial t$,

$$\gamma_{\sigma} = \frac{2\pi^2}{c^2} V_{\sigma} \sum_{s} Q^2_s e^2 \int\int d\mu \, dp \, p v^2 \frac{R^{\sigma}_{\mu\mu}}{(1 - \mu V_{\sigma}/v)^2} \left[\frac{\partial f_s}{\partial \mu} - \frac{V_{\sigma}}{v} \left(\mu \frac{\partial f_s}{\partial \mu} - p \frac{\partial f_s}{\partial p} \right) \right] \, . \tag{B14}$$

This is identical to equation (19) in the text apart from the use of particle momentum p instead of rigidity P.

APPENDIX C

DIFFUSION MODEL WITH STEADY MEAN FREE PATH

The particle density predicted by the radial diffusion model with mean free path $\lambda = \lambda_0 r^\beta$ ($\beta < 2$), for an impulsive release of N monoenergetic ions of velocity v at time $t = 0$ and $r = 0$, is (Parker 1963)

$$n(r,t) \equiv NG(r,t) = \frac{N}{4\pi\Gamma(\epsilon)}\left(\frac{\epsilon}{3}\right)^{2\epsilon-1}\left(\frac{3}{\lambda_0 vt}\right)^{\epsilon}\exp\left[-\frac{3r^{2-\beta}}{(2-\beta)^2\lambda_0 vt}\right], \tag{C1}$$

where

$$\epsilon = \frac{3}{2-\beta}. \tag{C2}$$

Let $n_{\rm X}(r,t)$ and $n_{\rm Y}(r,t)$ be the densities of X and Y ions in the form of equation (C1), with mean free paths $\lambda_{\rm X}$ and $\lambda_{\rm Y}$, respectively. Then the normalized Y/X ratio is given by

$$\frac{\rm Y}{\rm X} \equiv \frac{n_{\rm Y}/n_{\rm X}}{N_{\rm Y}/N_{\rm X}} = \frac{G_{\rm Y}}{G_{\rm X}} = \left(\frac{\lambda_{\rm X}}{\lambda_{\rm Y}}\right)^{3/(2-\beta)}\exp\left[\frac{3r^2}{(2-\beta)^2 vt}\left(\frac{1}{\lambda_{\rm X}}-\frac{1}{\lambda_{\rm Y}}\right)\right]. \tag{C3}$$

Suppose $\lambda_{\rm Y} > \lambda_{\rm X}$, e.g., Y = Fe^{+14}, X = O^{+7}, and λ increases with rigidity P in a Kolmogorov wave spectrum. Then equation (C1) predicts that the Y intensity rises earlier, peaks earlier, and decays faster than the X intensity. The normalized ratio Y/X in equation (C3) decreases monotonically from $\gg 1$ and asymptotes to a value less than 1, viz.,

$$\frac{\rm Y}{\rm X} \rightarrow \left(\frac{\lambda_{\rm X}}{\lambda_{\rm Y}}\right)^{3/(2-\beta)} < 1 \qquad \text{as } t \rightarrow \infty\,. \tag{C4}$$

For time-extended injections $S_{\rm Y}(t)$ and $S_{\rm X}(t)$ of energetic Y and X ions, respectively, the normalized ratio is given by

$$\frac{\rm Y}{\rm X} = \frac{\int_0^t d\tau\, G_{\rm Y}(r,\tau)S_{\rm Y}(t-\tau)}{\int_0^t d\tau\, G_{\rm X}(r,\tau)S_{\rm X}(t-\tau)}\,, \tag{C5}$$

where $G_{\rm Y}$ and $G_{\rm X}$ are Green's functions defined in equation (C1). In the case of steady injection at $t \gtrsim 0$, it can be shown from equations (C1) and (C5) without explicitly evaluating the integrals that

$$\frac{\rm Y}{\rm X} \rightarrow \frac{\lambda_{\rm X}}{\lambda_{\rm Y}} \qquad \text{as } t \rightarrow \infty\,, \tag{C6}$$

independent of β. This is in agreement with the result that may be obtained from the steady state solution of the diffusion model.

We have calculated via numerical convolution the intensities of X and Y ions and the Y/X ratio (eq. [C5]) in the diffusion model, for various identical and nonidentical time-extended injections and β indices of the two species. Large differences in the injection functions and/or β-values between the two species are needed to produce qualitatively different behavior in Y/X than described above. The ratio of A/Q values is 1.986 between He^{+2} and protons and $\lesssim 3$ between Fe and O ions for the likely charge states. Such small rigidity differences make it extremely unlikely that drastically different ion injections or mean free paths cause the observed time variations of SEP abundances (e.g., Tylka 2001).

With $D_{rr} = v\lambda/3$ as the radial diffusion coefficient, equation (C1) gives the following expression for the particle anisotropy:

$$\xi = -\frac{3D_{rr}}{vj_{E/A}}\frac{\partial j_{E/A}}{\partial r} = -\frac{\lambda}{f}\frac{\partial f}{\partial r} = \frac{3r}{(2-\beta)vt}\,, \tag{C7}$$

which is independent of λ. For time-extended injection it may be shown that $\xi > 3r/[(2-\beta)vt]$ and that ξ increases with λ.

REFERENCES

Achterberg, A., & Norman, C. A. 1980, A&A, 89, 353
Axford, W. I., Leer, E., & Skadron, G. 1977, Proc. 15th Int. Cosmic-Ray Conf. (Plovdiv), 11, 132
Barghouty, A. F., & Mewaldt, R. A. 2000, in AIP Conf. Proc. 528, Acceleration and Transport of Energetic Particles Observed in the Heliosphere, ed. R. A. Mewaldt, J. R. Jokipii, M. A. Lee, E. Möbius, & T. H. Zurbuchen (New York: AIP), 71
Barnes, A. 1992, J. Geophys. Res., 97, 1210
Bavassano, B., Dobrowolny, M., Mariani, F., & Ness, N. F. 1982, J. Geophys. Res., 87, 3617
Bell, A. R. 1978, MNRAS, 182, 147
Bieber, J. W., Matthaeus, W. H., Smith, C. W., Wanner, W., Kallenrode, M.-B., & Wibberenz, G. 1994, ApJ, 420, 294
Bieber, J. W., et al. 2002, ApJ, 567, 622
Boris, J. P., & Book, D. L. 1976, Methods Comput. Phys., 16, 85
Cane, H. V., Reames, D. V., & von Rosenvinge, T. T. 1988, J. Geophys. Res., 93, 9555
Desai, M. I., Mason, G. M., Dwyer, J. R., Mazur, J. E., Smith, C. W., & Skoug, R. M. 2001, ApJ, 553, L89
Dewar, R. L. 1970, Phys. Fluids, 13, 2710
Earl, J. A. 1974, ApJ, 193, 231
Eichler, D. 1981, ApJ, 244, 711

Ellison, D. C., & Ramaty, R. 1985, ApJ, 298, 400
Fisk, L. A., & Axford, W. I. 1968, J. Geophys. Res., 73, 4396
Forman, M. A., & Webb, G. M. 1985, in Collisionless Shocks in the Heliosphere: A Tutorial Review, ed. R. G. Stone & B. T. Tsurutani (Geophys. Monogr. 34; Washington, DC: AGU), 91
Gary, S. P. 1993, Theory of Space Plasma Microinstabilities (Cambridge: Cambridge Univ. Press)
Gordon, B. E., Lee, M. A., Möbius, E., & Trattner, K. J. 1999, J. Geophys. Res., 104, 28,263
Hasselmann, K., & Wibberenz, G. 1968, Z. Geophys., 34, 353
Isenberg, P. A. 1997, J. Geophys. Res., 102, 4719
Jokipii, J. R. 1966, ApJ, 146, 480
Kahler, S. W. 1994, ApJ, 428, 837
———. 2001, in Space Weather, ed. P. Song, H. Singer, & G. Siscoe (Geophys. Monogr. 125; Washington, DC: AGU), 109
Kahler, S. W., Sheeley, N. R., Jr., Howard, R. A., Koomen, N. J., Michels, D. J., McGuire, R. E., von Rosenvinge, T. T., & Reames, D. V. 1984, J. Geophys. Res., 89, 9683
Kennel, C. F., Coroniti, F. V., Scarf, E. L., Livesy, W. A., Russel, C. T., Smith, E. J., Wenzel, K.-P., & Scholer, M. 1986, J. Geophys. Res., 91, 11,917
Kulsrud, R. M., & Pearce, W. P. 1969, ApJ, 156, 445
Larson, D. J., Leske, R. A., Mewaldt, R. A., Stone, E. C., & von Rosenvinge, T. T. 1999, Proc. 26th Int. Cosmic-Ray Conf. (Salt Lake City), 7, 301
Leamon, R. J., Smith, C. W., Ness, N. F., Matthaeus, W. H., & Wong, H. K. 1998, J. Geophys. Res., 103, 4775
Lee, M. A. 1971, Plasma Phys., 13, 1079
———. 1982, J. Geophys. Res., 87, 5063
———. 1983, J. Geophys. Res., 88, 6109
———. 1997, in Coronal Mass Ejections, ed. N. Crooker, J. A. Jocelyn, & J. Feynman (Geophys. Monogr. 99; Washington, DC: AGU), 227
———. 2000, in AIP Conf. Proc. 528, Acceleration and Transport of Energetic Particles Observed in the Heliosphere, ed. R. A. Mewaldt, J. R. Jokipii, M. A. Lee, E. Möbius, & T. H. Zurbuchen (New York: AIP), 3
Lee, M. A., & Fisk, L. A. 1982, Space Sci. Rev., 32, 205
Lee, M. A., & Ryan, J. M. 1986, ApJ, 303, 829
Leske, R. A., Cummings, J. R., Mewaldt, R. A., Stone, E. C., & von Rosenvinge, T. T. 1995, ApJ, 452, L149
Lu, J. Y., Zank, G. P., & Webb, G. M. 2001, ApJ, 550, 34
Luhn, A., Klecker, B., Hovestadt, D., Scholer, M., Gloeckler, G., Ipavich, F. M., Fan, C. Y., & Fisk, L. A. 1984, Adv. Space Res., 4, 161
Mann, G., Classen, H.-T., & Motschmann, U. 2001, J. Geophys. Res., 106, 25,323
Mason, G. M., Gloeckler, G., & Hovestadt, D. 1983, ApJ, 267, 844
Mason, G. M., Mazur, J. E., & Dwyer, J. R. 1999, ApJ, 525, L133
Mason, G. M., Ng, C. K., Klecker, B., & Green, G. 1989, ApJ, 339, 529
Mazur, J. E., Mason, G. M., Looper, M. D., Leske, R. A., & Mewaldt, R. A. 1999, Geophys. Res. Lett., 26, 173
Melrose, D. B. 1980, Plasma Astrophysics, Vol. 1 (New York: Gordon & Breach)
Mewaldt, R. A., et al. 2001, Proc. 27th Int. Cosmic-Ray Conf. (Hamburg), 8, 3132
Möbius, E., et al. 2002, Adv. Space Res., 29, 1501
Ng, C. K., & Reames, D. V. 1994, ApJ, 424, 1032
———. 1995, ApJ, 453, 890
Ng, C. K., Reames, D. V., & Tylka, A. J. 1999a, Geophys. Res. Lett., 26, 2145
———. 1999b, Proc. 26th Int. Cosmic-Ray Conf. (Salt Lake City), 6, 151
———. 2001, Proc. 27th Int. Cosmic-Ray Conf. (Hamburg), 8, 3140
Ogilvie, K. W., Geiss, J., Gloeckler, G., Berdichevsky, D., & Wilken, B. 1993, J. Geophys. Res., 98, 3605
Ostryakov, V. M., Kartavykh, Y. Y., Ruffulo, D., Kovaltsov, G. A., & Kocharov, L. 2000, J. Geophys. Res., 105, 27,315
Parker, E. N. 1963, Interplanetary Dynamical Processes (New York: Wiley)
Potter, D. W. 1981, J. Geophys. Res., 86, 11,111
Reames, D. V. 1997, in Coronal Mass Ejections, ed. N. Crooker, J. A. Jocelyn, & J. Feynman (Geophys. Monogr. 99; Washington, DC: AGU), 227
———. 1999, Space Sci. Rev., 90, 413
———. 2002, ApJ, 571, L63
Reames, D. V., Barbier, L. M., & Ng, C. K. 1996, ApJ, 466, 473
Reames, D. V., & Ng, C. K. 1998, ApJ, 504, 1002
———. 2002, ApJ, 577, L59
Reames, D. V., Ng, C. K., & Berdichevsky, D. 2001, ApJ, 550, 1064
Reames, D. V., Ng, C. K., & Tylka, A. J. 1999, Geophys. Res. Lett., 26, 3585
———. 2000, ApJ, 531, L83
Rice, W. K. M., & Zank, G. P. 2000, in AIP Conf. Proc. 528, Acceleration and Transport of Energetic Particles Observed in the Heliosphere, ed. R. A. Mewaldt, J. R. Jokipii, M. A. Lee, E. Möbius, & T. H. Zurbuchen (New York: AIP), 147
Roelof, E. C. 1969, in Lectures in High-Energy Astrophysics, ed. H. Ogelman & J. R. Wayland (SP-199; Washington, DC: NASA), 111
Ruffolo, D. 1995, ApJ, 442, 861
———. 1997, ApJ, 481, L119
Ryan, J. M., Lockwood, J. A., & Debrunner, H. 2000, Space Sci. Rev., 93, 35
Sanderson, T. R., Reinhard, R., van Nes, P., Wenzel, K.-P., Smith, E. J., & Tsurutani, B. T. 1985, J. Geophys. Res., 90, 3973
Schlickeiser, R. 1989a, ApJ, 336, 243
———. 1989b, ApJ, 336, 264
Schlickeiser, R., & Achatz, U. 1993a, J. Plasma Phys., 49, 63
———. 1993b, J. Plasma Phys., 50, 85
Skilling, J. 1975, MNRAS, 172, 557
Stix, T. H. 1992, Waves in Plasmas (New York: AIP)
Tan, L. C., Mason, G. M., Gloeckler, G., & Ipavich, F. M. 1989, J. Geophys. Res., 94, 6552
Tsurutani, B. T., Smith, E. J., & Jones, D. E. 1983, J. Geophys. Res., 88, 5645
Tu, C.-Y., & Marsch, E. 1990, J. Plasma Phys., 44, 103
Tylka, A. J. 2001, J. Geophys. Res., 106, 25,333
Tylka, A. J., Boberg, P. R., McGuire, R. E., Ng, C. K., & Reames, D. V. 2000, in AIP Conf. Proc. 528, Acceleration and Transport of Energetic Particles Observed in the Heliosphere, ed. R. A. Mewaldt, J. R. Jokipii, M. A. Lee, E. Möbius, & T. H. Zurbuchen (New York: AIP), 147
Tylka, A. J., Cohen, C. M. S., Dietrich, W. F., MacLennan, C. G., McGuire, R. E., Ng, C. K., & Reames, D. V. 2001, ApJ, 558, L59
Tylka, A. J., Reames, D. V., & Ng, C. K. 1999, Geophys. Res. Lett., 26, 2141
Vainio, R., & Schlickeiser, R. 1999, A&A, 343, 303
Viñas, A. F., Goldstein, M. L., & Acuña, M. H. 1984, J. Geophys. Res., 89, 3762
Webb, G. M., Zakharian, A., Brio, M., & Zank, G. P. 1999, J. Plasma Phys., 61, 295
Wentzel, D. G. 1974, ARA&A, 12, 71
Witte, M., Wibberenz, G., Kunow, H., & Müller, R. 1979, Proc. 16th Int. Cosmic-Ray Conf. (Kyoto), 5, 79
Zank, G. P., Rice, W. K. M., & Wu, C. C. 2000, J. Geophys. Res., 105, 25,079
Zhou, Y., & Matthaeus, W. H. 1990, J. Geophys. Res., 95, 10,291